

# Supernova / Acceleration Probe: A Satellite Experiment to Study the Nature of the Dark Energy

G. Aldering<sup>1</sup>, W. Althouse<sup>2</sup>, R. Amanullah<sup>3</sup>, J. Annis<sup>4</sup>, P. Astier<sup>5</sup>, C. Baltay<sup>6</sup>, E. Barrelet<sup>5</sup>, S. Basa<sup>7</sup>, C. Bebek<sup>1</sup>, L. Bergström<sup>3</sup>, G. Bernstein<sup>8</sup>, M. Bester<sup>9</sup>, B. Bigelow<sup>10</sup>, R. Blandford<sup>2</sup>, R. Bohlin<sup>11</sup>, A. Bonissent<sup>12</sup>, C. Bower<sup>13</sup>, M. Brown<sup>10</sup>, M. Campbell<sup>10</sup>, W. Carithers<sup>1</sup>, E. Commins<sup>9</sup>, W. Craig<sup>2</sup>, C. Day<sup>1</sup>, F. DeJongh<sup>4</sup>, S. Deustua<sup>14</sup>, T. Diehl<sup>4</sup>, S. Dodelson<sup>4</sup>, A. Ealet<sup>7,12</sup>, R. Ellis<sup>15</sup>, W. Emmet<sup>6</sup>, D. Fouchez<sup>12</sup>, J. Frieman<sup>4</sup>, A. Fruchter<sup>11</sup>, D. Gerdes<sup>10</sup>, L. Gladney<sup>8</sup>, G. Goldhaber<sup>9</sup>, A. Goobar<sup>3</sup>, D. Groom<sup>1</sup>, H. Heetderks<sup>9</sup>, M. Hoff<sup>1</sup>, S. Holland<sup>1</sup>, M. Huffer<sup>2</sup>, L. Hui<sup>4</sup>, D. Huterer<sup>16</sup>, B. Jain<sup>8</sup>, P. Jelinsky<sup>9</sup>, A. Karcher<sup>1</sup>, S. Kent<sup>4</sup>, S. Kahn<sup>2</sup>, A. Kim<sup>1</sup>, W. Kolbe<sup>1</sup>, B. Krieger<sup>1</sup>, G. Kushner<sup>1</sup>, N. Kuznetsova<sup>1</sup>, R. Lafever<sup>1</sup>, J. Lamoureux<sup>1</sup>, M. Lampton<sup>9</sup>, O. Le Fèvre<sup>7</sup>, M. Levi<sup>1\*</sup>, P. Limon<sup>4</sup>, H. Lin<sup>4</sup>, E. Linder<sup>1</sup>, S. Loken<sup>1</sup>, W. Lorenzon<sup>10</sup>, R. Malina<sup>7</sup>, J. Marriner<sup>4</sup>, P. Marshall<sup>2</sup>, R. Massey<sup>17</sup>, A. Mazure<sup>7</sup>, T. McKay<sup>10</sup>, S. McKee<sup>10</sup>, R. Miquel<sup>1</sup>, N. Morgan<sup>6</sup>, E. Mörtzell<sup>3</sup>, N. Mostek<sup>13</sup>, S. Mufson<sup>13</sup>, J. Musser<sup>13</sup>, P. Nugent<sup>1</sup>, H. Oluseyi<sup>1</sup>, R. Pain<sup>5</sup>, N. Palaio<sup>1</sup>, D. Pankow<sup>9</sup>, J. Peoples<sup>4</sup>, S. Perlmutter<sup>1†</sup>, E. Prieto<sup>7</sup>, D. Rabinowitz<sup>6</sup>, A. Refregier<sup>18</sup>, J. Rhodes<sup>15</sup>, N. Roe<sup>1</sup>, D. Rusin<sup>8</sup>, V. Scarpine<sup>4</sup>, M. Schubnell<sup>10</sup>, M. Sholl<sup>9</sup>, G. Smadja<sup>19</sup>, R. M. Smith<sup>15</sup>, G. Smoot<sup>9</sup>, J. Snyder<sup>6</sup>, A. Spadafora<sup>1</sup>, A. Stebbins<sup>4</sup>, C. Stoughton<sup>4</sup>, A. Szymkowiak<sup>6</sup>, G. Tarlé<sup>10</sup>, K. Taylor<sup>15</sup>, A. Tilquin<sup>12</sup>, A. Tomasch<sup>10</sup>, D. Tucker<sup>4</sup>, D. Vincent<sup>5</sup>, H. von der Lippe<sup>1</sup>, J-P. Walder<sup>1</sup>, G. Wang<sup>1</sup>, W. Wester<sup>4</sup>

## ABSTRACT

The Supernova / Acceleration Probe (SNAP) is a proposed space-based experiment designed to study the dark energy and alternative explanations of the acceleration of the Universe's expansion by performing a series of complementary systematics-controlled astrophysical measurements. We here describe a

---

<sup>1</sup>Lawrence Berkeley National Laboratory

<sup>2</sup>Stanford Linear Accelerator Center

<sup>3</sup>University of Stockholm

<sup>4</sup>Fermi National Accelerator Laboratory

<sup>5</sup>LPNHE, CNRS-IN2P3, Paris, France

<sup>6</sup>Yale University

<sup>7</sup>LAM, CNRS-INSU, Marseille, France

<sup>8</sup>University of Pennsylvania

<sup>9</sup>University of California at Berkeley

<sup>10</sup>University of Michigan

<sup>11</sup>Space Telescope Science Institute

<sup>12</sup>CPPM, CNRS-IN2P3, Marseille, France

<sup>13</sup>Indiana University

<sup>14</sup>American Astronomical Society

<sup>15</sup>California Institute of Technology

<sup>16</sup>Case Western Reserve University

<sup>17</sup>Cambridge University

<sup>18</sup>CEA, Saclay, France

<sup>19</sup>IPNL, CNRS-IN2P3, Villeurbanne, France

self-consistent reference mission design that can accomplish this goal with the two leading measurement approaches being the Type Ia supernova Hubble diagram and a wide-area weak gravitational lensing survey. This design has been optimized to first order and is now under study for further modification and optimization. A 2-m three-mirror anastigmat wide-field telescope feeds a focal plane consisting of a 0.7 square-degree imager tiled with equal areas of optical CCDs and near infrared sensors, and a high-efficiency low-resolution integral field spectrograph. The instrumentation suite provides simultaneous discovery and light-curve measurements of supernovae and then can target individual objects for detailed spectral characterization. The SNAP mission will discover thousands of Type Ia supernovae out to  $z = 3$  and will obtain high-signal-to-noise calibrated light-curves and spectra for a subset of  $> 2000$  supernovae at redshifts between  $z = 0.1$  and  $1.7$  in a northern field and in a southern field. A wide-field survey covering one thousand square degrees in both northern and southern fields resolves  $\sim 100$  galaxies per square arcminute, or a total of more than 300 million galaxies. With the PSF stability afforded by a space observatory, SNAP will provide precise and accurate measurements of gravitational lensing. The high-quality data available in space, combined with the large sample of supernovae, will enable stringent control of systematic uncertainties. The resulting data set will be used to determine the energy density of dark energy and parameters that describe its dynamical behavior. The data also provide a direct test of theoretical models for the dark energy, including discrimination of vacuum energy due to the cosmological constant and various classes of dynamical scalar fields. If we assume we live in a cosmological-constant-dominated Universe, the matter density, dark energy density, and flatness of space can all be measured with SNAP supernova and weak-lensing measurements to a systematics-limited accuracy of 1%. For a flat universe, the density-to-pressure ratio of dark energy or equation of state  $w(z)$  can be similarly measured to 5% for the present value  $w_0$  and  $\sim 0.1$  for the time variation  $w' \equiv dw/d \ln a|_{z=1}$ . For a fiducial SUGRA-inspired universe,  $w_0$  and  $w'$  can be measured to an even tighter uncertainty of 0.03 and 0.06 respectively. Note that no external priors are needed. As more accurate theoretical predictions for the small-scale weak-lensing shear develop, the conservative estimates adopted here for space-based systematics should improve, allowing even tighter constraints. While the survey strategy is tailored for supernova and weak gravitational lensing observations, the large survey area, depth, spatial resolution, time-sampling, and nine-band optical to NIR photometry will support additional independent and/or complementary dark-energy measurement approaches as well as a broad range of auxiliary science programs.

*Subject headings:* Early universe—instrumentation: detectors—space vehicles: instruments—supernovae:general—telescopes

## 1. Introduction

In the past decade the study of cosmology has taken its first major steps as a precise empirical science, combining concepts and tools from astrophysics and particle physics. The most recent of these results have already brought surprises. The Universe’s expansion is apparently accelerating rather than decelerating as expected due to the gravitational attraction of matter. This implies that the flat, matter-dominated model for the Universe does not apply and that our current fundamental physics understanding of particles, forces, and fields is likely to be incomplete.

This evidence for a vacuum energy, or more generally a negative-pressure component called “dark en-

ergy”, comes from the supernova measurements of changes in the Universe’s expansion rate that directly show the acceleration. Figure 1 shows the results of Knop et al. (2003) (see also Tonry et al. (2003)) which compare the standardized brightnesses of ground and space-observed high-redshift ( $0.18 < z < 0.863$ ) Type Ia supernovae (SNe Ia) with a large sample of low-redshift SNe Ia (Hamuy et al. 1996b; Riess et al. 1999). The data implies that for a flat universe a fraction  $\Omega_\Lambda = 0.75 \pm 0.07$  of the critical density would reside in a cosmological constant. More generally, these measurements indicate the presence of a new, unknown energy component with energy density  $\Omega_w$  that can cause acceleration, hence having an equation of state (ratio of pressure to energy density (Turner & White 1997)) with  $w \equiv p/\rho < -1/3$ .

---

\*Co-PI, email: melevi@lbl.gov

†PI, email: saul@lbl.gov

The evidence for dark energy has received strong corroboration from cosmic microwave background (CMB) results (Balbi et al. 2000; Lange et al. 2001b; Spergel et al. 2003) which are sensitive to the total energy density, combined with galaxy power spectrum and cluster abundance measurements (Bahcall et al. 1999; Efstathiou et al. 2002; Percival et al. 2002; Allen et al. 2003) which probe the matter density  $\Omega_M$ , or with an  $H_0$  prior (see Figure 1). Two of these three independent measurements would have to be in error to make dark energy unnecessary in the cosmological model.

The dark energy might be due to the cosmological constant term in Einstein’s equations, which implies vacuum energy with  $w = -1$ . Alternatively, it could be due to a dynamical scalar field with  $w \neq -1$  and/or time-varying  $w$ . The fundamental importance of a universal vacuum energy has sparked a flurry of activity in theoretical physics with several classes of models being proposed (e.g. quintessence (Ratra & Peebles 1988; Caldwell et al. 1998; Ferreira & Joyce 1998), Pseudo-Nambu-Goldstone Boson (PNGB) models (Frieman et al. 1995; Coble et al. 1997), cosmic defects (Vilenkin 1984; Vilenkin & Shellard 1994), and modified gravity (Dvali et al. 2000; Carroll et al. 2003).

All these models explaining the accelerating Universe have observational consequences for the supernova Hubble diagram (Weller & Albrecht 2002). The luminosity distance as a function of redshift can for convenience be parameterized to first order with effective dark-energy parameters, e.g.  $w_{const}$ , or  $w_0, w_a$ . A constant  $w_{const}$  can represent dark-energy models such as the cosmological constant while  $w = w_0 + w_a(1 - a)$  is successful at describing a wide variety of both scalar field and more general models (Linder 2003a, 2004). Predictions of dark-energy models can be either compared directly to supernova Hubble diagrams or to the dark-energy parameters as fit by the data. Placing some constraints on possible dark-energy models, Perlmutter et al. (1999b); Garnavich et al. (1998); Perlmutter et al. (1999a); Knop et al. (2003) find that for a flat universe, the data are consistent with a cosmological-constant equation of state and  $0.2 \lesssim \Omega_M \lesssim 0.4$  (Figure 2), or generally  $w_{const} < -0.6$  at 95% confidence level. When combining supernova with other results, such as from a variety of CMB experiments and large-scale-structure measurements (Hawkins et al. 2003; Spergel et al. 2003), Knop et al. (2003) find  $w_{const} = -1.05^{+0.15}_{-0.20} (\pm 0.09$

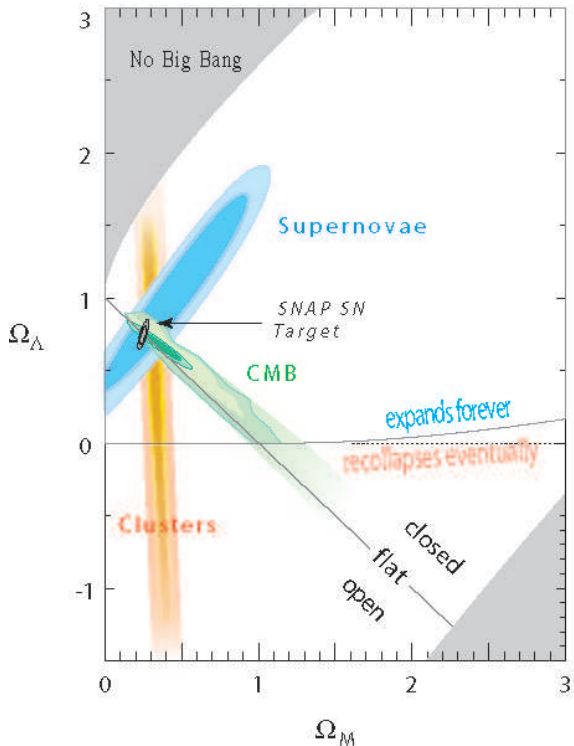


Fig. 1.— There is strong evidence for the existence of a cosmological vacuum energy density. Plotted are  $\Omega_M$ — $\Omega_\Lambda$  68% and 95% confidence regions for supernovae (Knop et al. 2003), cluster measurements (based on Allen et al. (2003)), and CMB data with  $H_0$  priors (outer contours from Lange et al. (2001a), inner contours from Spergel et al. (2003)). These results rule out a simple flat  $\Omega_M = 1, \Omega_\Lambda = 0$  cosmology. Their consistent overlap is a strong indicator for dark energy. Also shown is the expected confidence region from just the SNAP supernova program for  $\Omega_M = 0.28, \Omega_\Lambda = 0.72$ .

systematics) and Riess et al. (2004) get  $w_{const} = -1.02^{+0.13}_{-0.19}$ . Cosmic strings ( $w = -1/3$ ) are already ruled out as dark energy, while the domain walls ( $w = -2/3$ ) and tracking quintessence models ( $w \gtrsim -0.7$ ) are disfavored.

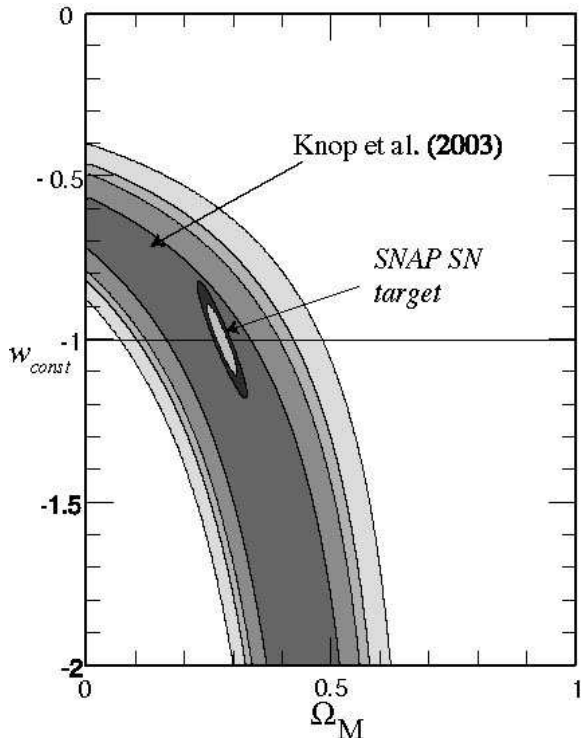


Fig. 2.— Best-fit 68%, 90%, 95%, and 99% confidence regions in the  $\Omega_M$ - $w$  plane for an additional energy density component,  $\Omega_w$ , characterized by an equation-of-state  $w = p/\rho$  using supernovae alone (Knop et al. 2003). The fit is constrained to a flat cosmology ( $\Omega_M + \Omega_w = 1$ ). Also shown are the expected 68% and 95% confidence regions allowed by just the SNAP supernova program assuming the fiducial values  $w = -1$  and  $\Omega_M = 0.28$ .

Current and upcoming ground-based supernova experiments will continue to improve measurements of the dynamical effects of the dark energy. For example, the Nearby Supernova Factory (Aldering et al. 2002) will produce a photometrically calibrated spectral time-series for hundreds of  $0.03 < z < 0.08$  supernovae, providing a rich data set for refining our understanding of SN Ia behavior. The SNLS<sup>1</sup> and

<sup>1</sup><http://snls.in2p3.fr/>

Essence<sup>2</sup> projects will discover and follow hundreds of supernovae to  $\sim 0.03 - 0.05$  mag accuracy in the range  $z = 0.3 - 0.7$ , giving significantly tighter constraints on the value of  $w_{const}$ . Unfortunately once the assumption that  $w$  is constant is relaxed, these experiments are not able to provide strong constraints on  $w_0$  nor  $w'$  (Perlmutter & Schmidt 2003). Testing the nature of dark energy will thus be difficult with these experiments.

A new experiment is then necessary to study the properties and possible models for the dark energy, and refine the measurement of the matter and dark energy densities of the Universe. Since the discovery of cosmic acceleration in 1998, many observational approaches to dark energy have been proposed (see Kujat et al. (2002); Tegmark (2002); Linder (2003b); Cooray et al. (2004) for recent reviews). The most well developed and understood method of constructing the expansion history of the Universe is the same one that led to the discovery of dark energy: the measurement of the supernova Hubble diagram. The systematic and statistical uncertainties in current SN Ia measurements are on the same order of magnitude: any new experiment to perform precision cosmology must eliminate or significantly reduce the influence of the systematic uncertainties while discovering and measuring high-quality light curves and spectra of a statistically large number of supernovae.

In this paper we describe the Supernova/Acceleration Probe (SNAP), a dedicated satellite mission designed to measure the properties of dark energy. Originally conceived in 1999 (Perlmutter 1999), the SNAP concept has progressed through a series of refinements all starting with science requirements and then deriving observational, instrumental, and mission requirements. The SNAP reference mission is presented in this paper in the form of a spacecraft, orbit, telescope, imager, spectrograph, and observation strategy. This mission serves as a reference from which future optimization studies will be performed and is a demonstration of a design that can realistically accomplish the science goals. It is self-consistent, technically feasible, reduces risk, and is specifically designed to provide data that strictly control statistical and systematic uncertainties for supernova and weak gravitational lensing science.

SNAP can run as a complete supernova experiment providing discovery, and photometric and spec-

<sup>2</sup><http://www.ctio.noao.edu/essence/>

trosopic followup of a full sample of supernovae over the target redshifts. SNAP is also an excellent platform for performing deep wide-field surveys with space-quality imaging providing crucial complementary constraints to study dark energy from weak lensing and other studies. SNAP’s full potential is realized when used in conjunction with complementary results that are anticipated by the time SNAP launches: a large sample of well-measured low-redshift SNe Ia and precise measurements of the distance to the surface of last scattering from the Planck satellite.

In §2 we describe the precision cosmology that can be achieved using Type Ia supernovae. The needed supernova data set is based on the identification of known or plausible systematic uncertainties that fundamentally limit measurement accuracy, and on the number and redshift range of supernovae necessary to probe precisely the dark-energy parameters. The power of weak gravitational lensing surveys in measuring cosmological parameters is discussed in §3 and the added complementarity of lensing and other dark-energy probes made possible with SNAP data is described in §4. We present in §5 the observing strategies and instrumentation suite tailored to provide the data that satisfy both the statistical and systematic requirements for the supernova and lensing surveys. The SNAP calibration program is described in §6. The results of detailed simulations of the SNAP mission are given in §7. In §8 we discuss the general properties of the SNAP surveys and the science resources they will provide.

## 2. Cosmology with Supernovae

Type Ia SNe have already proved to be excellent distance indicators for probing the dynamics of the Universe. However, the current supernova cosmology measurements are limited by systematic uncertainties (which occur for all cosmological probes). In order to move toward the era of precision cosmology, a new data set must both address potential systematic uncertainties and provide sufficient statistical power to accurately determine dark-energy properties, especially the time variation of the equation of state. Because control of systematic uncertainties is so central we begin with aspects of the data set necessary for their control. We proceed by listing the sources of systematic uncertainty, strategies to reduce their effects, and the resulting improvements that can be obtained in measuring the supernova Hubble diagram. We then deter-

mine which supernova observations give a statistical uncertainty comparable to the systematic uncertainty, leading to requirements on the number of supernovae we need to find, their distribution in redshift, and how precisely we need to determine each one’s peak brightness.

### 2.1. Control of Systematic Uncertainties

#### 2.1.1. Known Sources of Systematic Uncertainties

High-redshift supernova searches have been proceeding since the late 1980’s (Norgaard-Nielsen et al. 1989; Couch et al. 1989; Perlmutter et al. 1995, 1997, 1998, 1999b; Schmidt et al. 1998; Riess et al. 1998; Tonry et al. 2003; Knop et al. 2003; Riess et al. 2004). Particularly since the discovery of the accelerating expansion of the Universe, the high-redshift supernova methodology for measuring cosmological parameters has been critically scrutinized for sources of systematic uncertainty. Below are identified systematic effects which any experiment aiming to make maximal use of the supernova technique will need to recognize and control. We also give a rough estimate of the expected *systematic* residual in supernova magnitude after statistical correction for such effects with the SNAP data set or from independent data sets from other astrophysical studies.

*Extinction by Host-galaxy “Normal” Dust:* Extinction from host-galaxy dust can significantly reduce the observed brightness of a discovered supernova although typically Type Ia supernovae suffer only modest extinction (Hatano et al. 1998). Cross-wavelength flux-calibrated spectra and multi-band photometry will identify the properties of the obscuring dust and gas and the amount of extinction suffered by individual supernovae. There will remain a residual uncertainty proportional to the calculated extinction due to dust-model dependence. This can be minimized by excluding highly-extincted supernovae from the analysis. Stringent requirements on the SNAP calibration system are needed to control uncertainties in the photometric-system zeropoints, particularly since the uncertainties are correlated from supernova to supernova. Our calibration program is being designed to control extinction uncertainty to 1%.

*Gravitational Lensing by Clumped Mass:* Inhomogeneities along the supernova line of sight can gravitationally magnify or demagnify the supernova flux and shift the mode of the supernova magnitude distribution by  $\sim 1 - 10\%$  depending on redshift (Holz & Wald

1998; Mörtzell et al. 2001; Amanullah et al. 2003). Since flux is conserved in this process, averaging large numbers of supernovae per redshift bin will give the correct mean brightness. Deviations from a Gaussian distribution for the brightness of supernovae at similar  $z$  can be used to determine the clumpiness of the intervening mass distribution (Kim et al. 2004). The large SNAP supernova sample will reduce the distance modulus uncertainty per redshift bin to  $\sim 0.5\%$ . SNAP weak gravitational lensing measurements, and microlensing studies can further help distinguish whether or not the matter is in compact objects.

*K-Correction and Cross-Filter Calibration:* Broadband photometry of supernovae at different redshifts is sensitive to differing supernova-rest-frame spectral regions. K-corrections are used to put these differing photometry measurements onto a consistent rest-frame passband (Kim et al. 1996; Nugent et al. 2002). Applying K-corrections with only today’s methods and calibration sets could produce errors of several percent. Using the currently available spectra, we tune the SNAP filter-set specifications to give the target systematic uncertainty  $< 0.02$  mag. (The situation will improve even further as the spectral library of supernovae grows and SNAP itself will add to this library.) Furthermore, strict requirements are placed on the SNAP calibration program to ensure accurate transformations of fluxes between filters.

*Galactic Extinction:* Extinction maps of our own Galaxy are uncertain by  $\sim 1$ –10% depending on direction (Schlegel et al. 1998). Supernova fields can be chosen toward the low extinction Galactic caps. Future Spitzer observations will allow an improved mapping between color excesses (e.g. of Galactic halo subdwarfs in the SNAP field) and Galactic extinction by dust. Galactic-extinction uncertainty can then be controlled to  $< 0.5\%$  in brightness.

*Non-SN Ia Contamination:* Other supernova types are on average fainter than SNe Ia and their contamination could bias their Hubble diagram. Observed supernovae must be positively identified as SN Ia. As some Type Ib and Ic supernovae have spectra and brightnesses that otherwise mimic those of SNe Ia, a spectrum covering the defining rest frame Si II 6150Å feature for every supernova at maximum will provide a pure sample. This systematic would then be eliminated.

*Malmquist Bias:* A flux-limited sample preferentially detects the intrinsically brighter members of any population of sources. The amount of magnitude bias

depends on details of the search but can reach the level of the intrinsic magnitude dispersion of a standard candle. Directly correcting this bias would rely on knowledge of the SN Ia luminosity function, which may change with lookback time. A detection threshold fainter than peak by at least five times the intrinsic SN Ia luminosity dispersion ensures sample completeness with respect to intrinsic supernova brightness, eliminating this bias (Kim et al. 2004).

### 2.1.2. Possible Sources of Systematic Uncertainties

A systematics-limited experiment must account for speculative but reasonable sources of uncertainty. The following are sources of systematic uncertainty for which there is no direct evidence but which cannot yet be discounted.

#### *Extinction by Gray Dust*

As opposed to normal dust, gray dust is postulated to produce wavelength-independent absorption in optical bands (Aguirre 1999; Aguirre & Haiman 2000). Although models for gray-dust grains dim blue and red optical light equally, the near-infrared (NIR) light ( $\sim 1$ – $2 \mu\text{m}$ ) is less affected. Cross-wavelength calibrated spectra extending to wavelength regions where “gray” dust is no longer gray will characterize the hypothetical large-grain dust’s absorption properties. Armed with the extinction – color excess properties of the gray dust, broadband near-infrared colors can provide “gray” dust extinction corrections for supernovae out to  $z = 0.5$ ; Goobar et al. (2002a) have explored the observations necessary to be sensitive to 0.02 mag gray-dust extinction.

Gray dust will re-emit absorbed starlight and thus contribute to the far-infrared background; current observations indicate that the FIR flux is attributable to point sources (Borys et al. 2002; Scott et al. 2002). Quasar colors in the SDSS sample as a function of redshift give an upper limit to the possible dimming due to gray dust at the level of 0.2 mag (in the rest-frame B-band) at  $z = 1$  (Mörtzell & Goobar 2003). Deeper SCUBA and Spitzer observations should further tighten the constraints on the amount of gray dust allowed.

#### *Uncorrected Supernova Evolution*

Supernova behavior itself may have systematic variations depending, for example, on properties of the

progenitor systems. The distribution of these stellar properties is likely to change over time—“evolve”—in a given galaxy, and over a population of galaxies. Supernova heterogeneity manifests itself through observed signatures in their spectral light emission (the bulk emitted in optical wavelengths), and the time-evolution of that emission. Signs of supernova diversity are thus captured in observations of multi-band light curves and/or spectral time-sequences that begin shortly after explosion and extend to the nebular phase of the event. This has been done using optical measurements of nearby SNe Ia drawn from a wide range of galactic environments that provide an observed evolutionary range of SNe Ia (Hamuy et al. 1996a, 2000). The photometric and spectral differences that have been identified in these data are well calibrated by the SN Ia light curve width-luminosity relation, leaving a 10% intrinsic peak-brightness dispersion. There is currently no evidence for systematic residuals after correction, for example with galaxy type or supernova location (Sullivan et al. 2003).

High signal-to-noise ( $S/N$ ) multi-band light curves and spectra over optical wavelengths can provide precise control over additional general supernova variability. Efforts are underway to expose additional effects using larger, more precise and systematic, low-redshift supernova surveys (Aldering et al. 2002). These high-quality data are also necessary to control possible evolution effects when performing precision cosmology with high-redshift supernovae.

Theoretical models can identify observables that are expected to display heterogeneity. These key features, indicative of the underlying initial conditions and physical mechanisms controlling the supernova, will be measured with SNAP, allowing statistical correction for what would otherwise be a systematic uncertainty. The state of empirical understanding of these observables at the time SNAP launches will be explicitly tested by SNAP measurements (Branch et al. 2001). At present, we perform Fisher matrix analyses on model spectra and light curves to estimate the statistical measurement requirements, and to ensure that we have necessary sensitivity to use subsamples to test for residual systematics at better than the 2% level. This approach reveals the main effects of — as well as the covariance between — the following observables:

*Rise time from explosion to peak:* This is an indicator of opacity, fused  $^{56}\text{Ni}$  mass, and possible differences in the  $^{56}\text{Ni}$  distribution. A 0.1 day uncertainty corresponds to a 1% brightness constraint at peak (Höflich

et al. 1998). Achieving such accuracy requires discovery within  $\sim 2$  days of explosion, on average,  $\sim 30\times$  fainter than peak brightness. Current constraints on rise-time differences are two days (Aldering et al. 2000).

*Plateau level 45 days past peak:* The light-curve plateau level that begins  $\sim 45$  days past — and more than  $10\times$  fainter than — peak is an important indicator of the C/O ratio of the progenitor star, and fused  $^{56}\text{Ni}$ . In models, a 5% constraint on this plateau brightness corresponds to a 1% constraint on the peak brightness (Höflich et al. 1998).

*Overall light-curve timescale:* The “stretch factor” (Goldhaber et al. (2001), see also Riess et al. (1996); Perlmutter et al. (1997); Phillips et al. (1999)) that parameterizes the light-curve timescale (Phillips 1993) is affected by almost all of the aforementioned parameters since it tracks the SN Ia’s light-curve development from early to late times. It is correlated with rise time and plateau level and it ties SNAP’s controls for systematics to the controls used in the current ground-based work. A 0.5% uncertainty in the stretch factor measurement corresponds to a  $\sim 1\%$  uncertainty at peak (Perlmutter et al. 1999b). Stretch distributions are quite consistent between the current sets of low and high-redshift supernovae (Perlmutter et al. 1999b; Knop et al. 2003).

*Spectral line velocities:* The velocities of several spectral features throughout the UV and visible make an excellent diagnostic of the kinetic-energy injection in SNe Ia. In models, velocities constrained to  $\sim 250 \text{ km s}^{-1}$  constrain the peak luminosity to  $\sim 1\%$  (Höflich et al. 1998), given a typical SNe Ia expansion velocity of  $15,000 \text{ km s}^{-1}$ . Current data show smooth velocity development for a given supernova, but also clear differences between supernovae which have not yet been found to correlate with supernova luminosity (Branch & van den Bergh 1993; Hatano et al. 2000).

*Spectral features:* The positions of various spectral features in the restframe UV are strong metallicity indicators of the SNe Ia. By achieving a sufficient  $S/N$  and resolution on such features (Bernstein & Kim 2004) SNAP will be able to constrain the metallicity of the progenitor to 0.1 dex (Lentz et al. 2000). This spectral region has only recently begun to be explored with UV spectroscopy of nearby supernovae with HST. Spectral features in the restframe optical (Ca II H&K and Si II at  $6150 \text{ \AA}$ ) provide additional constraints on the opacity and luminosity of the SN Ia (Nugent et al. 1995).

Figures 3 and 4 show the particular light-curve and spectral parameters that can serve as indicators of supernova evolution. By measuring all of the above features for each supernova we can tightly constrain the physical conditions of the explosion. This makes it possible to recognize subsets of supernovae with matching initial conditions, ensuring a small luminosity range for each subset.

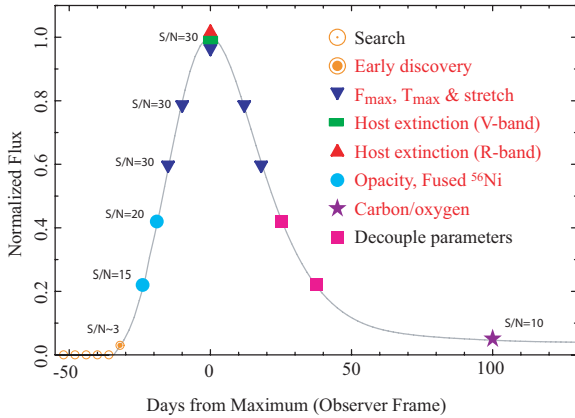


Fig. 3.— Sample B-band light curve for a  $z = 0.8$  Type Ia supernova. Signal-to-noise targets are shown at different epochs for identification of possible systematic effects.

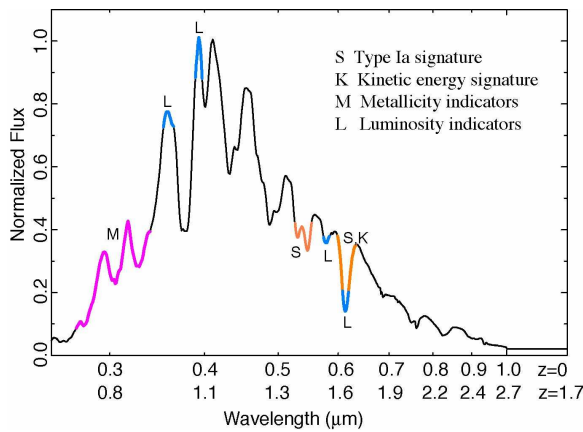


Fig. 4.— Type Ia spectra at maximum light showing line features associated with possible Type Ia supernova variation. The horizontal axis shows observer frame wavelengths for  $z = 0$  and  $z = 1.7$  supernovae.

In addition to these features of the supernovae themselves, we will also study the host galaxy of the

supernova. We can measure the host galaxy luminosity, colors, morphology, and the location of the supernova within the galaxy, even at redshifts  $z \sim 1.7$ . The last two observations are difficult or impossible from the ground for high-redshift galaxies. These galaxy properties can provide clues to any shifts with redshift in the supernova progenitor population.

### 2.1.3. Systematic-Error Model

The behavior of systematic uncertainties are complicated and the determination of their propagated effects on cosmology requires rigorous analysis (Kim et al. 2004; Huterer et al. 2004). Particularly important systematic effects for supernova-cosmology experiments are those that put a floor on how well the distance modulus can be measured in a certain redshift bin. For example, supernovae at similar redshifts whose rest-frame flux regions lie in common observer passbands can share completely correlated calibration uncertainty. An increase in the statistical sample of supernovae cannot decrease this uncertainty. In addition, these uncertainties could be correlated across redshift bins. Again taking calibration as an example, a temperature uncertainty in a blackbody fundamental calibrator propagates into correlated flux and magnitude zeropoint uncertainties. Correlated errors across redshift bins can lead to a bias in the determination of the cosmological and dark-energy parameters. We do not further consider correlated bias in this paper as Kim et al. (2004) find that the systematic bias in  $w_0$  and  $w'$  lies well within the 68%-error contours due to comparably-sized irreducible systematic uncertainties.

For convenience we adopt in this paper a systematic-uncertainty model of  $0.02(1.7/z_{max})(1+z)/2.7$  magnitude irreducible uncertainty per redshift bin of width 0.1 as proposed by Linder & Huterer (2003), where  $z_{max}$  represents the depth of the survey. The systematic uncertainty introduced in the comparison of high-redshift supernovae with the local sample is an increasing function of redshift. Systematic uncertainty will exist at some level even for the local sample, due for example to uncertainty in the Galactic-extinction zeropoint and spatial correlations in  $E(B - V)$  maps.

## 2.2. Comparing Defined Subsets of Supernovae

The subtyping strategy employed for evolution based on observables tied to the explosion characteristics can be more generally applied. The data (supernova risetime, early detection, light-curve peak-to-tail

ratio, identification of the Type Ia-defining Si II spectral feature, separation of supernova light from host-galaxy light, and identification of host-galaxy morphology, etc.) make it possible to study each individual supernova and measure enough of its physical properties to recognize deviations from standard brightness subtypes. Only the change in brightness as a function of the parameters classifying a subtype is needed, not any intrinsic brightness. Supernovae cannot change their brightness in one measured wavelength range without affecting brightness somewhere else in the spectral time series — an effect that is well-captured by expanding atmosphere computer models.

As a precision experiment SNAP is designed to distinguish supernovae “demographics” by detecting subtle variations in light-curve and spectral parameters. By matching like to like among the supernova subtypes we can construct independent Hubble diagrams, each with systematic biases reduced to the level of 1% in distance. This procedure is described and tested in Kim et al. (2004). Comparison within a redshift bin reveals possible systematics, while comparison within a subtype over the redshift range cleanly probes the cosmology.

The targeted residual systematic uncertainty from effects such as Malmquist bias,  $K$ -correction, etc. total  $\sim 2\%$ . Thus, a subset, or “like vs. like”, analysis based on physical conditions should group supernovae to within  $< 2\%$  in luminosity. This is in addition to a purely statistical correction for any second-parameter effects beyond the stretch factor.

### 2.3. Supernova Sample to Probe Dark Energy

The statistical supernova sample appropriate for experiments with the presence of systematic uncertainty has been considered in the Fisher-matrix analysis of Linder & Huterer (2003). (Their results have been validated with our independent Monte Carlo analysis.) They assign a statistical uncertainty of 0.15 magnitudes to each supernova, which combines statistical measurement uncertainty and intrinsic supernova dispersion. The systematic-error model described in §2.1.3 is included.

The importance of using SNe Ia over the full redshift range out to  $z \sim 1.7$  for measuring the cosmological parameters is demonstrated in Figure 5, which shows the uncertainty in measuring the equation of state parameter variation,  $w'$ , as a function of maximum redshift probed in distance surveys (Linder &

Huterer 2003). (Note that the results look very similar whether one defines  $w'$  in terms of a linear expansion of  $w(z)$  in redshift or in scale factor, and whether one uses a prior on matter density or on distance to the CMB last scattering surface.) This calculation considers 2000 SNe Ia measured in the range  $0.1 \leq z \leq z_{\max}$ , along with 300 low-redshift SNe Ia from the Nearby Supernova Factory (Aldering et al. 2002). A flat universe is assumed. Three types of experiments were considered. The first is an idealized experiment subject only to statistical uncertainties, free of any systematics, and with extremely tight prior knowledge of the matter density. The second two are more realistic models which assume both statistical and systematic uncertainties and different priors on  $\Omega_M$ .

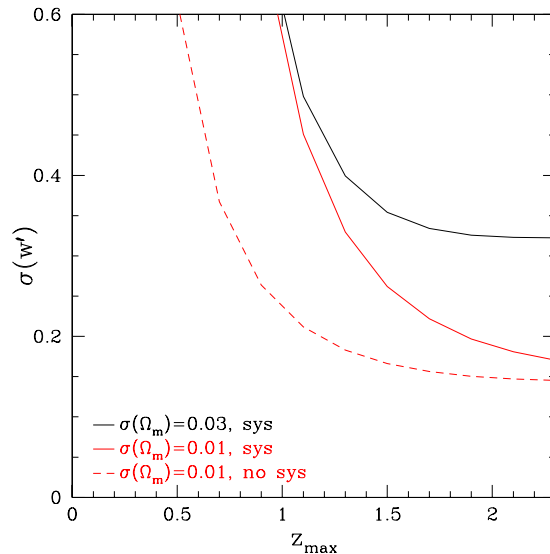


Fig. 5.— From Linder & Huterer (2003), accuracy in estimating the equation of state variation parameter,  $w'$ , as a function of maximum redshift probed in supernova distance surveys. The lower two curves assume priors in  $\Omega_M$  good to 0.01, while the upper two curves are for the case where systematic uncertainties are present. The top, heavy curve corresponds to the most realistic case. It is clear that even with modest systematic uncertainties good accuracy requires probing to high redshift. In all cases a flat universe is assumed.

From this figure we conclude that a SN Ia sample extending to redshifts of  $z > 1.5$  is crucial for realistic experiments in which some systematic uncertainties

remain after all statistical corrections are applied. Ignoring systematic uncertainties can lead to claims that are too optimistic. Similar conclusions apply for the other dark-energy parameters, including  $w_0$  and an assumed constant  $w$  (Linder & Huterer 2003).

The sample of  $\sim 2000$  SNe Ia is enough to provide systematic-uncertainty limited measures of the dark-energy parameter  $w'$ . These supernovae represent a subset of SNe Ia that can provide robust cosmological measurements (e.g. non-peculiar, low-extinction), culled from an even larger set of discovered supernovae. This large sample is necessary to allow model-independent checks for any residual systematics or refined standardization parameters, since the sample will have to be subdivided in a multidimensional parameter space of redshift, light curve-width, host properties, etc. The large number of lower signal-to-noise light curves from supernovae at  $z > 1.7$  will provide an extended redshift bin in which to check for consistency with the core sample.

Expected parameter measurement precisions for the SNAP supernova program with  $z_{max} = 1.7$  are summarized in Table 1. We determine precisions for two fiducial flat universes with  $\Omega_M = 0.3$ , one in which the dark energy is attributed to a Cosmological Constant and the other to a SUGRA-inspired dark-energy model. The parameter precisions then depend on the choice of data set, priors from other experiments, assumptions on the flatness of the universe, and the model for the behavior of  $w$ . (Parameter determination from Monte Carlo analysis of simulated data from the reference SNAP mission is given in §7.)

If the universe is taken to be spatially flat, the SN data (with Planck prior) determine  $\Omega_M$  to 0.01. The present value of the dark energy equation of state is constrained within 0.09 and the physically crucial dynamical clue of the equation of state time variation is bounded to within 0.19. Note that these constraints are *systematics limited*; much tighter constraints would be obtained if systematics were ignored. (In §4 we discuss the tighter constraints obtained by combining the supernova results with the other SNAP measurements.)

The precise, homogeneous, deep supernova data set allows for robust interpretation in more general terms than  $w_0$  and  $w'$ . The function  $w(z)$  can be implemented in a nonparametric, uncorrelated bin, or eigenmode method (Huterer & Starkman 2003; Huterer & Cooray 2004). One can also obtain the expansion history  $a(t)$  itself, e.g. Linder (2003a).

We can also obtain constraints on flatness of the universe, rather than assuming it. Current data are mostly sensitive to one linear combination of  $\Omega_M$  and  $\Omega_\Lambda$  (roughly their difference). SNAP is designed to obtain sufficient brightness-redshift data for a wide range of redshifts ( $0.1 < z < 1.7$ ), and to enable an extraordinarily accurate measurement of  $\Omega_M$  and  $\Omega_\Lambda$  separately (see Figure 1), the culmination of an approach originally proposed by Goobar & Perlmutter (1995). Assuming that the dark energy is the cosmological constant, the supernova experiment can simultaneously determine the mass density  $\Omega_M$  to an accuracy of 0.02, the cosmological constant energy density  $\Omega_\Lambda$  to 0.05. Propagating this through one obtains a 0.06 measurement uncertainty of the curvature of the universe,  $\Omega_k = 1 - \Omega_M - \Omega_\Lambda$ .

### 3. Cosmology with Weak Lensing

Gravitational weak lensing provides an independent and complementary measurement of the dark-energy parameters through the mapping of galaxy-shape distortions induced by mass inhomogeneities in the Universe. Weak gravitational lensing of background galaxies by foreground dark matter (large-scale structure) provides a direct measurement of the amount and distribution of dark matter (see §8.2 for details on the impact SNAP can have on these measurements). The growth of these dark matter structures with cosmic time is determined by the dark energy. Thus, precise weak lensing observations can provide significant and independent constraints on the properties of dark energy. For a review of the techniques used to measure weak lensing and the current status of weak-lensing measurements, see Refregier (2003).

#### 3.1. Weak Lensing as a Probe of Dark Energy

Dark energy modifies the weak-lensing observables by altering the distance-redshift relation as well as the matter power spectrum. These two, in turn, determine the weak-lensing shear power spectrum (Kaiser 1998). Specifically, dark energy will modify the normalization and nonlinear part of the matter power spectrum and redshift evolution. Weak lensing measurements with a wide-field space telescope such as SNAP can thus achieve an accurate measurement of  $\Omega_w$ , and the dark-energy parameters (Hu 1999; Huterer 2002; Abazajian & Dodelson 2003; Refregier et al. 2004).

In Figure 6 we show the expected measurement of the shear power spectrum possible with 100 million

TABLE 1

SNAP 1- $\sigma$  UNCERTAINTIES IN DARK-ENERGY PARAMETERS, WITH CONSERVATIVE SYSTEMATICS FOR THE SUPERNOVA AND A 1000 SQ. DEG. WEAK-LENSING SURVEY. NOTE: THESE UNCERTAINTIES ARE SYSTEMATICS-LIMITED, NOT STATISTICS LIMITED.

	$\sigma_{\Omega_M}$	$\sigma_{\Omega_w}$	$\sigma_{w_0}$	$\sigma_{w'}$
<hr/> <hr/> Fiducial Universe: flat, $\Omega_M = 0.3$ , Cosmological Constant dark energy <hr/>				
SNAP SN; $w = -1$	0.02	0.05	...	...
SNAP SN + WL; $w = -1$	0.01	0.01	...	...
SNAP SN; $\sigma_{\Omega_M} = 0.03$ prior; flat; $w(z) = w_0 + 2w'(1 - a)$	...	0.03	0.09	0.31
SNAP SN; Planck prior; flat; $w(z) = w_0 + 2w'(1 - a)$	...	0.01	0.09	0.19
SNAP SN + WL; flat; $w(z) = w_0 + 2w'(1 - a)$	...	0.005	0.05	0.11
<hr/> <hr/> Fiducial Universe: flat, $\Omega_M = 0.3$ , SUGRA-inspired dark energy <hr/>				
SNAP SN; $\sigma_{\Omega_M} = 0.03$ prior; flat; $w(z) = w_0 + 2w'(1 - a)$	...	0.03	0.08	0.17
SNAP SN; Planck prior; flat; $w(z) = w_0 + 2w'(1 - a)$	...	0.02	0.09	0.13
SNAP SN + WL; flat; $w(z) = w_0 + 2w'(1 - a)$	...	0.005	0.03	0.06

NOTE.—Cosmological and dark-energy parameter precisions for two fiducial flat universes with  $\Omega_M = 0.3$ , one in which the dark energy is attributed to a Cosmological Constant and the other to a SUGRA-inspired dark-energy model. The parameter precisions then depend on the choice of data set, priors from other experiments, assumptions on the flatness of the universe, and the model for the behavior of  $w$ . In this paper we adopt the non-standard definition  $w' \equiv dw/d \ln a|_{z=1}$

galaxies over 300 square degrees divided into 2 redshift bins. The upper curve represents a measurement using resolved source galaxies with  $z > 1$  while the lower curve represents  $z < 1$  galaxies. The power of space-based observations is most apparent at small scales (high  $\ell$ ), where the shot noise is small due to the large surface density of resolved galaxies. In Figure 7 we show the joint constraints on  $\Omega_M$  and assumed-constant  $w$  using 10 million galaxies, 100 million galaxies, and 100 million galaxies divided into two redshift bins with additional skewness information. Note that the constraints from weak lensing are largely orthogonal to the constraints from supernovae. Thus, weak lensing complements the supernova technique in deriving constraints on  $w$ .

Takada & Jain (2003) have demonstrated that by combining additional information on non-Gaussianity from the lensing bispectrum in the moderately non-linear regime with the power spectrum, cosmological constraints can be improved significantly (about a fac-

tor of three over the results shown in Figure 7). At present the ability to exploit this information is limited by computationally intensive numerical predictions for non-linear growth, but the gravitational physics involved is well understood and work on obtaining accurate predictions is already underway.

At still smaller (arcminute) angular scales, the lensing signal is very strong, but the non-linear growth predictions become very difficult. New statistical treatments of weak-lensing data have recently been proposed (Jain & Taylor 2003; Bernstein & Jain 2004) which measure the cosmic geometry while canceling uncertainties in the non-linear growth. This is achieved by cross-correlating the lensing signal with an estimate of the foreground mass distribution. Figure 8 presents an estimate by Bernstein & Jain (2004) of the statistical uncertainties on  $w_0$  and  $w_a$  (or  $w'$ , recall  $w_a \sim 2w'$  at  $z \sim 1$ ) that could be obtained by the SNAP surveys using this lensing cross-correlation technique. The quality of the measurement is compa-

erable to that of the Type Ia SN measurements, as long as the systematic uncertainties are kept below the statistical uncertainties.

### 3.2. Advantages of Space-Based Measurements

Several conditions are necessary to make possible high signal-to-noise weak-lensing measurements for these types of analyses. The shapes of millions of background galaxies must be measured to overcome cosmic variance and provide a precise measure of the dark matter power spectrum. It is particularly important to be able to resolve many small, distant galaxies beyond a redshift of  $z \simeq 1$ ; the broad redshift range of source galaxies provides a powerful lever arm on the constraint of  $w$  by providing information on the growth of structure. High spatial resolution is necessary to extract statistically powerful shape information from each individual galaxy and decrease the size of the smallest resolved galaxies in a survey. A stable point spread function (PSF) and a minimal level of internal

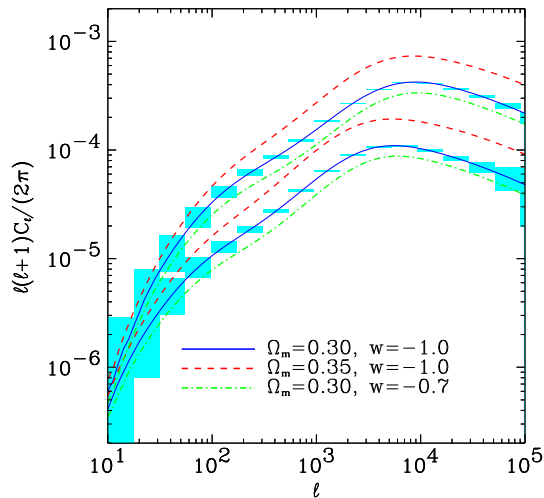


Fig. 6.— The dark matter power spectrum in two redshift intervals. The upper curve represents a measurement made with lens galaxies at  $z > 1$  and the lower curve a measurement with  $z < 1$ . Three different cosmological models are shown. It is clear that the over 100 million resolved galaxies in the SNAP wide survey will distinguish between cosmological models even after being divided into redshift intervals. Therefore, high signal-to-noise measurements of the evolution of the power spectrum will be possible.

optical distortions are essential for the precise measurement of galaxy shapes. The high spatial density of resolved background galaxies afforded by space-based observations allows cross-correlation measurements and gives measurements of the mass power spectrum at scales where non-linearities are most apparent. Accurate photometric redshifts are required for the lensing analyses, particularly the lensing cross-correlation, where any systematic biases in photo- $z$ 's above  $\sim 0.001$  in  $\log(1+z)$  would dominate the error budget. Catastrophic photo- $z$  errors would similarly need to be kept below 1 per 1000. It may be possible use internal analyses of lensing data to trade precision on the dark energy parameters for looser constraints on photo- $z$  biases. Reducing the photo- $z$  errors, biases, and catastrophic errors requires high-accuracy photometry in bands spanning the visible and near-IR. Atmospheric emission lines make it impractical to acquire these data in the near-IR and near certain bright

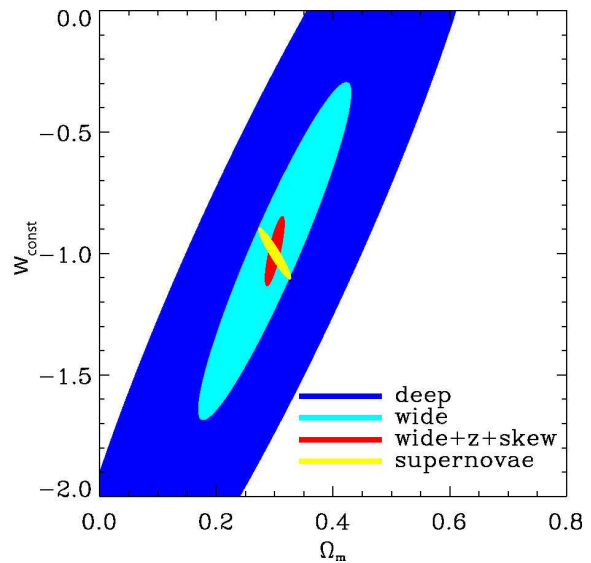


Fig. 7.— Joint constraints on  $\Omega_M$  and  $w_{const}$  achievable with the SNAP deep and wide surveys using weak gravitational lensing. The blue contour is for the SNAP supernova survey and cyan contour for the wide-field survey. After dividing the wide survey into two redshift intervals and adding skewness information, the constraints (the red contour) are similar in size to the SN Ia constraints (shown as a yellow ellipse). Since weak-lensing constraints are largely orthogonal to those of SNe Ia, weak lensing plays a crucial role in SNAP's ability to measure dark energy.

visible lines.

Satisfying all of these requirements simultaneously requires a wide-field space based imaging telescope in a thermally stable orbit. With a high-throughput, space-based 2 meter telescope, an exposure time of 2000s will provide the depth to resolve significant numbers of galaxies in the scientifically interesting range beyond  $z \simeq 1$ . Unhindered by atmospheric emission and absorption, NIR observations from space provide significant redshift depth and improved photometric redshift estimates. Avoiding the Earth’s atmosphere in a thermally stable orbit gives the fine resolution and stable PSF. The PSF and depth give a high galaxy surface density. A ground-based survey of tens of thousands of square degrees, exploring the mass power spectrum on large angular scales with small statistical errors would be complementary. In particular, such large-angular-scale surveys probe the linear part of the matter power spectrum while deeper but somewhat less wide surveys probe the nonlinear region. (For completeness, we discuss the possibility of

a panoramic, wide-field survey with SNAP in §5.1.3.)

#### 4. Joint SNAP Constraints on Dark Energy from Weak-lensing, Supernova, and other Measurements

The two complementary cosmological surveys that constitute the leading components of the SNAP primary mission together combined give constraints on the properties of dark energy significantly stronger than either one by itself. Table 1 gives the expected dark-energy parameter uncertainties from the joint results from the deep supernova survey and the combination of power spectrum, bispectrum, and cross-correlation cosmography techniques from a 1000 square-degree lensing program with  $n_{gal} = 100 \text{ arcmin}^{-2}$ . A very conservative estimate of the systematics floor on shear calibration of 3% is used.

For a flat universe the present dark energy equation of state  $w_0$  can be measured to  $\pm 0.05$ , and the time variation can be bounded within 0.11. Without assuming a flat universe, the mass density  $\Omega_M$ , the cosmological constant energy density  $\Omega_\Lambda$ , and curvature  $\Omega_k$  can be determined to  $\lesssim 0.01$ . This poses an interesting test of the cosmological framework by cross-checking the curvature measured at  $z \sim 1$  with current measurements out to  $z \sim 1000$  of  $\Omega_k = -0.02 \pm 0.02$  (Bennett et al. 2003). Note that *no priors* are required when we consider the full SNAP mission of supernovae plus weak lensing. These are significant improvements over the results from supernovae alone. The constraints are subject to improvement as practical understanding of future weak lensing data develops.

Universes with more dark energy (than the fiducial  $\Omega_{DE} = 0.7$  assumed here), dark energy possessing a more positive equation of state or a stronger time variation would lead to a measurement with more sensitivity to dark-energy properties. We have been conservative in taking the cosmological constant as fiducial, the least sensitive of the canonical quintessence models. For example, in a supergravity-inspired model of dark energy (Brax & Martin 2000),  $w'$  would be more tightly constrained to  $\pm 0.06$ . With strong constraints on  $w'$  we will be able to differentiate between the cosmological constant and a range of dynamical scalar-field (“quintessence”) particle-physics models (Weller & Albrecht (2001, 2002); Huterer & Turner (2001).)

The SNAP reference mission focuses on the established methods of Type Ia supernova Hubble diagrams and weak gravitational lensing to study dark

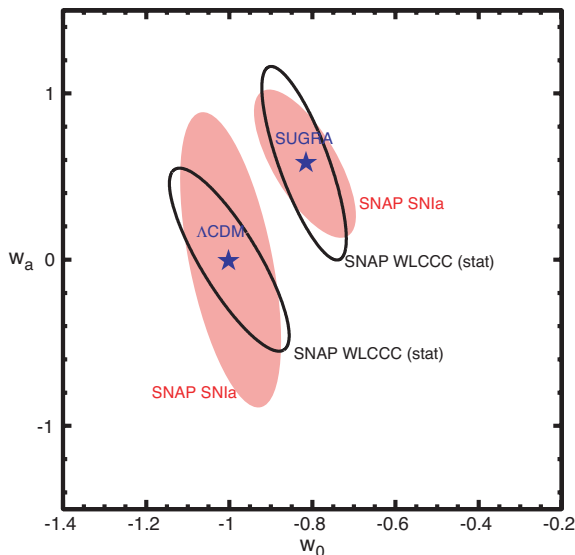


Fig. 8.— Constraints on the parameters  $w_0$  and  $w_a \approx 2w'$ , where  $w(z) = w_0 + w_a(1 - a)$  and  $a$  is the scale factor (Linder 2003a). Shown are the SNAP constraints from the supernova survey (filled contours), and those from weak-lensing cross-correlation cosmography (empty contours; statistics only), as discussed in the text. We show constraints for two models: vacuum energy (“ $\Lambda$ CDM”) and a supergravity-inspired model (“SUGRA”) (Brax & Martin 2000).

energy. Other less-tested and more model-dependent methods for measuring cosmological parameters are now being explored as additional probes of dark energy with SNAP. These include (but are not limited to) using Type II supernovae as distance indicators (Kirshner & Kwan 1974; Baron et al. 1993; Baron et al. 1995; Leonard et al. 2003), baryon oscillations as a standard ruler in both transverse and radial directions (Seo & Eisenstein 2003), redshift-space correlations for the Alcock-Paczynski test (Matsubara & Szalay 2003), strong lensing time-delays and statistics (Holz 2001; Goobar et al. 2002b), and cluster-counting statistics (Haiman et al. 2001). Attacking dark energy with measurements from independent techniques that are subject to differing, but tightly controlled systematic uncertainties will give increased confidence in the ultimate conclusions made about its nature. Since these techniques generally constrain different combinations of cosmological parameters, it is important that each “stand on its own two feet” with systematics control so that they can be combined for studies of dark energy.

SNAP can naturally study dark energy using many of these other probes. The necessary measurements can be made with the SNAP instrumentation suite as is, or in coordination with ground or other space-based telescopes. A SNAP panoramic-survey observing mode that covers a significant fraction of sky can provide large number statistics, redshift depth, wavelength coverage, discovery of rare objects, and measures on large angular scales; these are exactly the characteristics of the data needed for many of these complementary methods, with all the advantages of observations above the distorting and absorbing atmosphere.

## 5. Reference Model SNAP Experiment

Discovery and study of a larger number and of more distant supernovae (or any probe) is by itself insufficient to successfully accomplish a rigorous investigation of the cosmological model. As shown in §2.1 we must address each of the systematic concerns while making precise supernova measurements, thus requiring a major leap forward in measurement techniques. The requirements placed on the SNAP instrument derive directly from the science goals.

The primary requirement is to obtain the corrected peak brightness vs. redshift of at least 2000 Type Ia SNe out to a redshift of  $z = 1.7$ . Identification of

Type Ia SNe requires the measurement of characteristic spectral features near peak luminosity. Host-galaxy redshift is also determined spectroscopically. The corrected peak magnitudes are derived from supernova rest-frame optical light curves and spectra. We require a statistical measurement uncertainty for the peak magnitude corrected for extinction and shape inhomogeneity roughly equal to the current intrinsic magnitude dispersion of supernovae,  $\sim 0.1$  mag, and a systematic uncertainty almost an order of magnitude smaller.

To meet the scientific requirements, the SNAP reference mission has a large, 0.7 square degree instrumented field of view and an observing cadence of 4 days, commensurate with the timescale over which early-epoch supernova light curves change. The imager’s large field-of-view gives a significant multiplex advantage; each exposure contains  $\sim 80$  Type Ia supernovae within 5.4 observer-frame months from the date of explosion (corresponding to 2 rest-frame months for  $z = 1.7$  supernovae). Observations in multiple filters yield multi-color rest-frame optical light curves. A spectrometer optimized for supernova spectra is allocated observation time for supernova type-identification, feature measurements, and spectral-template building. The telescope aperture is constrained by the photometric and spectroscopic  $S/N$  requirements and the focal plane must accommodate the large field of view.

The derived requirements for the SNAP reference mission described here serve as a starting point; they are subject to change as the mission is further refined. As other subsidiary approaches to measure dark energy are developed as discussed in §4 we can also consider minor detector additions or replacements on the focal plane with either extended broad-band filters or with dispersive elements. For example, a band in between the reference filter bands could sharpen the photometric redshift accuracy for a part of the survey field. As a general rule, broadband photometry is significantly faster than slitless spectroscopy by the ratio  $R_{spect}/R_{filter}$  for equivalent  $S/N$ , however, for specific applications a detector with a small dispersive element in place of a filter may be useful. It could provide spectral time series of core-collapse supernovae that fall in the limited field enabling the determination of their distance. It could also provide precise redshifts of field sources that can calibrate photometric redshifts – especially useful for tomographic weak lensing, or for the baryon-oscillation method.

## 5.1. Reference Model Observation Strategy and Data Package

The primary SNAP science program consists of a deep survey and a wide-field survey with individually-designed observing schedules. The repeated scans of the deep-survey field provide supernova discovery and light curves, and when coadded give a high surface density of background galaxies for lensing surveys. The wide-field survey is designed for dark-energy measurements using weak lensing and other  $w$ -sensitive techniques. In addition, we explore a possible panoramic survey that extends the weak-lensing data and provides the general astronomical community a “legacy” survey of space-quality optical-to-NIR images of a significant fraction of the sky. The programs are described here and summarized in Table 2. The surveys are described by the solid-angle of sky monitored, the exposure time for each scan of the field, and the number of times the survey region is scanned.

### 5.1.1. Supernova Program

A simple, predetermined observing strategy repeatedly steps through a 7.5 square degree northern zone with a 4 day cadence continuing for 16 months. Later in the mission this strategy is repeated for a southern survey region. The fields are selected to be perpendicular to the Sun, Earth, and Moon and where natural zodiacal light is near minimum, toward the north and south ecliptic caps. This deep-survey strategy allows discovery and automatic followup for SNe Ia that explode in those regions. Every field will be visited every four days for 16 months, with sufficiently long exposures that all relevant SNe Ia in the SNAP survey regions will have significant signal within a few rest-frame days of explosion. (supernovae at much higher redshifts on average will be found slightly later in their light curve rise times although their prior history is in the data.) The periodic observation of fixed fields ensures that every supernova at  $z < 1.7$  will have its light curve followed for at least several months in the rest frame as it brightens and fades.

Sixty percent of the SNAP deep supernova survey will be spent for the pure photometric scan; about 120 exposures are possible with a four day cadence to cover a scan area of 7.5 square degrees. Running this survey again in the south yields another 7.5 square degrees.

The zodiacal light will be the dominant source of background given SNAP’s fields, orbit, and shielding

of sun and earthshine. The cosmic-ray flux<sup>3</sup> contamination of 4.5 particles/cm<sup>2</sup>/s will make multiple exposures necessary to eliminate significant contamination of the images.

Forty percent of the SNAP deep survey will be spent doing targeted spectroscopy of supernovae with parallel imaging (that is, imaging occurs simultaneously during these spectroscopic observations). The resulting images will cover random positions and orientations within the SNAP field and will be used to increase the depth of the survey and help with photometric and astrometric cross-calibration between detectors.

This prearranged observing program will provide a uniform, standardized, calibrated data set for each supernova, allowing for the first time comprehensive comparisons across complete sets of SNe Ia. The following reference strategies and measurements will address, and often eliminate, the statistical and systematic uncertainties described in § 2.1.

- Blind, multiplexed searching.
- SNe Ia at  $0.1 \leq z \leq 1.7$ .
- Spectrum for every supernova at maximum covering the rest frame UV and Si II 6150Å feature.
- Spectral time series of representative SN Ia, with cross-wavelength relative flux calibration.
- Light curves sampled at frequent, standardized intervals starting shortly after explosion and extending to 80 restframe days after explosion to obtain a light-curve-width- and extinction-corrected peak rest-frame  $B$  brightness to 10%. This requires percent-level peak-magnitude determinations in the supernova-frame optical passbands.
- Multiple color measurements in a filter set consisting of 9 bands approximating rest-frame  $B$  at different redshifts.
- Final images and spectra after the supernova is no longer present to enable clean subtraction of host galaxy light.

The quality of these measurements is as important as the time and wavelength coverage, so we require control over  $S/N$  for these photometry and spectroscopy measurements to give high statistical significance for supernovae over the entire range of redshifts.

<sup>3</sup>From <http://crsp3.nrl.navy.mil/creme96/>

TABLE 2  
REFERENCE SNAP SURVEYS.

Program	Solid Angle Per Filter (sq. deg.)	Exposure Per Scan (s)	Cadence (days)	# Scans
Deep North	7.5	Optical: $4 \times 300$ NIR: $8 \times 300$	4	120
Wide-field	300 – 1000	Optical: $6 \times 200$ NIR: $12 \times 200$	...	1
Deep South	7.5	Optical: $4 \times 300$ NIR: $8 \times 300$	4	120
Panoramic	7000 – 10000	Optical: $6 \times 67$ NIR: $12 \times 67$	...	1

We also require control over calibration for these photometry and spectroscopy measurements, by collecting monitoring data to measure cross-instrument and cross-wavelength calibration.

Note that to date no single SN Ia has ever been observed with this complete set of calibrated measurements, either from the ground or in space, and only a handful have a data set that is comparably thorough. With the observing strategy described here, *every one* of  $> 2000$  followed SN Ia will have this complete set of measurements.

The requirements on spectroscopic exposure times and signal-to-noise are described in detail in Bernstein & Kim (2004). Using an exposure time of 8.5 hours for  $z = 1.7$  supernovae will provide the desired spectral-parameter measurements given the SNAP spectrograph parameters described in §5.5. Exposure times for supernovae at lower redshifts down to  $z \sim 1$  obey a scaling factor of  $(1 + z)^6$ . The exact exposure time necessary will be refined as the library of UV–optical supernova spectra continues to grow in coming years.

The number of supernovae that SNAP is expected to discover is based on the supernova rate per unit volume of Pain et al. (2002) assumed independent of redshift, which when extrapolated is roughly consistent with the discoveries of the GOODS/ACS search and Subaru supernova search. This is a conservative assumption compared to rates calculated incorporating the cosmic star formation rate (Madau et al. 1998). SNAP will be able to spectroscopically observe almost all the supernovae with deep and good temporal photometric coverage,  $\sim 4000$  supernovae in the 32-month survey. Frieman et al. (2003) find that in a

resource-limited survey with systematic uncertainties taken into account, using a relatively uniform distribution at high redshift is optimal for providing cosmological parameter measurements. As a result, SNAP will not provide spectroscopic followup for a fraction of the highest redshift supernovae, which are more plentiful than the lower redshift supernovae. For the cosmology analysis, we expect to cull the sample of spectroscopically observed supernovae to  $\sim 2000$  events that satisfy strict homogeneity and extinction cuts to yield a flat distribution in cosmic time as shown in Figure 9.

#### 5.1.2. Weak-Lensing Program

The strengths that make SNAP excellent for supernova observations apply to lensing as well; a wide-field imager in space with stable and narrow point-spread-functions can provide large survey areas, accurate shape measurements, and high galaxy angular-surface densities. The nine optical and near infrared filters are necessary for accurate photometric redshift determinations. The SNAP deep-survey fields in which the supernovae are found will thus serve as a deep lensing field. The SNAP wide-field survey has been tailored to resolve the shapes of  $\sim 100$  galaxies per square arcminute. Over one year  $\sim 300$  million galaxies will be resolved. For source galaxies with an intrinsic ellipticity distribution  $\sigma_\epsilon = 0.31$  (Rhodes et al. 2000), this will achieve a signal-to-noise of unity on the shear measurement in a 1 square arcminute cell, over 1000 square degrees. The reference SNAP deep survey will exceed even this density requirement by a factor of three (Massey et al. 2004).

Current plans for the wide-field survey call for each

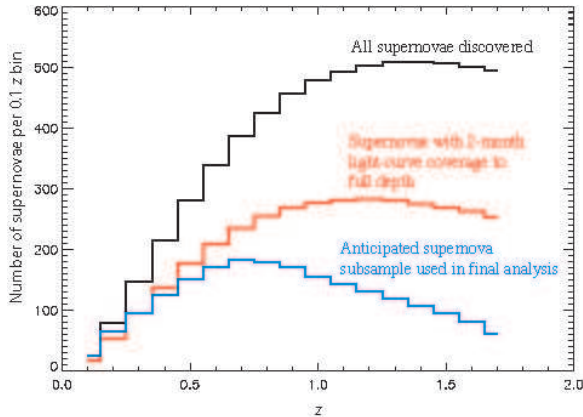


Fig. 9.— Close to 6000 Type Ia supernovae will explode in the SNAP field of view out to  $z = 1.7$  during the course of the SNAP deep survey (upper black curve). A subset of these will be observed in all filters to full depth and early enough during the survey to be followed photometrically for at least two months in the supernova frame (middle red curve). Most of these objects will be observed spectroscopically. A smaller subset of supernovae with homogeneous light curves and spectra will be used in the final cosmology analysis; we anticipate using a flat distribution in cosmic time (bottom blue curve).

field to be observed for 1200 seconds in each optical filter, and twice as long in each NIR filter. Each pointing will be divided up into 6 individual 200 second exposures which are needed to eliminate cosmic rays and cover the spatial gaps between the detectors. We are engaged in determining the systematic uncertainties intrinsic to the SNAP weak-lensing program to find the optimal survey area and allotted time for the wide-field survey; initial estimates indicate 300-1000 square degree field (5–16 months) are appropriate for the wide-field survey.

The on-board storage space is matched to the telemetry and these two constraints limit how many images can be stored and subsequently sent to Earth. If the telemetry constraints can be eased, either through a higher download rate (and greater on-board storage) or through data compression, the exposure times can be made shorter, thus increasing the area of the weak lensing survey.

A full description of the SNAP weak-lensing program can be found in a separate series of papers (Rhodes et al. 2004; Massey et al. 2004; Refregier

et al. 2004).

### 5.1.3. Panoramic Survey

A extremely wide-field “panoramic” imaging survey is potentially useful for weak lensing and other probes of dark energy, cosmology, and astronomy in general. SNAP will provide a unique means for performing wide-field optical imaging from space. We thus explore the depth obtained from a three-year SNAP survey covering 7000–10000 square degrees. We do not address specific scientific programs made possible from this survey, considering it as a possible legacy dataset that can serve the astronomical community at large.

## 5.2. Orbit

The reference mission calls for a halo orbit about the second earth-sun Lagrange point (L2). The L2 point is about 1.5 million kilometers from the earth along the sun-earth line and has a very stable thermal environment. There are no eclipses and heat from the earth is constant and negligible. There are ample communication contact opportunities from the ground to SNAP. A ground station would communicate from 2-4 hours per day with the spacecraft. This orbit is highly advantageous from the standpoint of achieving passive detector cooling; a three square meter radiator that operates at 130K provides 45 watts of gross cooling capacity.

Having the SNAP fields near the ecliptic caps places the Sun at nearly right angles to the viewing direction throughout the year. In an L2 orbit, the Earth and Moon will always be nearly at right angles to the viewing direction and on the sun side of the spacecraft. We utilize this viewing geometry in several ways. First, the solar panels can be rigidly body-mounted on the sunward side of the spacecraft, avoiding the cost, failure modes, and flexure of deployed panels. Second, the passive cooling radiator can be rigidly located in permanent shadow on the anti-sunward side of the spacecraft. Third, the stray light baffling can be optimized for a limited range of solar roll and elevation angles, and for a limited range of Earth elevation angles.

We plan to have the spacecraft perform 90 degree roll maneuvers every 3 months during the mission, to keep up with the mean ecliptic longitude of the Sun. The detector layout in the focal plane has a 90 degree roll symmetry that allows photometric scans with iden-

tical filter coverage from season to season (see §5.4).

### 5.3. Telescope

The requirements placed on the SNAP telescope derive directly from the science goals and the mission constraints. The wavelength coverage is determined by the need to observe a number of filter bands across the visible and NIR wavelength range spanning over  $0.35\ \mu\text{m}$  to  $1.7\ \mu\text{m}$ , and to conduct low-resolution spectroscopy of each supernova near maximum light. This requirement effectively rules out refracting optical trains and drives the telescope design toward all-reflective optics.

The light gathering power is set by the need to discover supernovae early in their expansion phases and to permit photometry and low-resolution spectroscopy near maximum light. These requirements can be met with a minimum aperture of about two meters. Note that for a fixed signal-to-noise ratio ( $S/N$ ) the exposure time for an isolated point source is proportional to the telescope aperture to the fourth power with background-limited noise and diffraction-limited optics.

Image quality is also a factor in determining  $S/N$  because of the effects of natural zodiacal light and detector noise. We intend to achieve angular resolution near the diffraction limit for wavelengths longward of one micron. For a two-meter aperture and one-micron wavelength the Airy disk size is  $0.11''$  FWHM. To match this diffraction spot size to the CCD pixel size ( $\sim 10\ \mu\text{m}$ ) one must adopt an effective focal length of about 20 meters. This focal length is also matched in the NIR where HgCdTe detectors with  $18\text{--}20\ \mu\text{m}$  pixels will observe out to a photon wavelength of  $17000\ \text{\AA}$ .

A large field of view is needed to obtain multiplexing advantage: a single exposure can contain tens of different supernovae that are in important phases of their light curves. The SNAP reference mission has a field of view of the order one square degree, of which about  $0.7$  square degrees will be instrumented by detector pixels. The ratio of working field area to diffraction patch area is about 800 million, comparable to the total number of detector pixels.

An excellent optical quality and low-level of distortion must be maintained over the working focal plane. The image quality of the telescope is driven in part by the  $S/N$  requirement, and also by the potential systematic supernova spectrum contamination by un-

wanted light from the supernova host galaxy. A system Strehl ratio of  $0.90$  at one micron wavelength is baselined, which corresponds to an RMS wavefront error (WFE) of  $0.05\ \mu\text{m}$ . At  $0.633\ \mu\text{m}$  the Strehl ratio is  $0.77$ . (The Strehl ratio is the peak monochromatic image irradiance divided by the theoretical peak irradiance for the ideal diffraction limited image.)

#### 5.3.1. Optical Configuration

Prospective launch vehicles (Delta IV, ATLAS V, SeaLaunch) and payload fairing dimensions impose limits on the telescope size and its mass. An overall payload length of about 6 meters and a payload diameter of about 2.5 meters will accommodate the SNAP observatory. Through a series of packaging exercises we have explored ways to fit the maximum length stray light baffle into available launch fairings, and find that with a short optical package,  $\sim 3\ \text{m}$  in length, and a tall outer baffle, the required stray light rejection can be achieved (§5.3.6).

To accommodate dimensional limitations and wide-field optical quality, the three mirror anastigmat described by Korsch (1977) is used. A schematic view is shown in Figure 10.

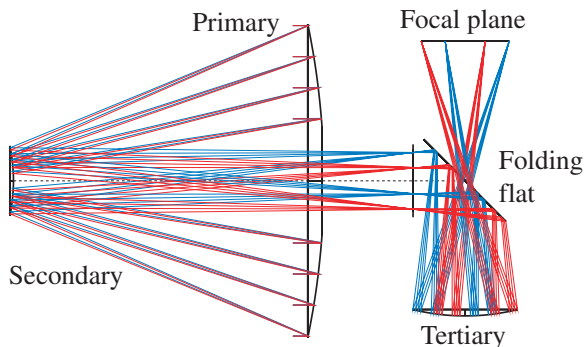


Fig. 10.— Reference model SNAP optics layout. The entrance pupil is defined by the 2-m primary mirror. The exit pupil is at the folding mirror.

Details of the reference SNAP optical configuration have been determined by an iterative process involving exploring various alternative choices for focal length, working field coverage, and packaging constraints (Lampton et al. 2002b, 2003). The optimized optical parameters are summarized in Table 3. The overall length of the optical train is 3.3 meters. Compared with the 21.66 meter effective focal length, this system has an effective telephoto advantage of about

6.5. The mirrors are pure conic sections of revolution having no polynomial terms. The use of higher polynomial terms has not yet been explored. The location of the vertex of each element is listed in a Cartesian (X,Z) coordinate system whose origin is the vertex of the primary mirror and Z is the optical axis.

### 5.3.2. Mechanical Configuration

The launch environment imposes both stiffness and strength requirements on the payload. Vehicle aeroelastic stability concerns prescribe the needed payload stiffness in terms of minimum structural frequencies in the axial ( $\sim 25$  Hz) and lateral ( $\sim 10$  Hz) directions. The launch environment includes both quasi-steady and random acceleration events that are combined to establish the peak loads, or strength requirements for the payload.

For a space mission it is vital to create a mechanical configuration which provides an extremely stable metering structure that maintains the optical element alignment during ground testing, launch, and orbit operations. The concept adopted for SNAP is to create three structural components that will be brought together during spacecraft/payload integration: a stiff low-precision outer baffle cylinder carrying the exterior solar panels and extensive thermal insulation; a stiff low-precision spacecraft bus structure that carries antennas, batteries, and other major spacecraft support components; and a stiff high-precision telescope structure comprising carbon-fiber metering elements, the kinematically-mounted mirrors, the instrumentation suite, and its own thermal control system. Figure 11 shows the overall payload and spacecraft layout, while Figure 12 shows details of the secondary and tertiary metering structures.

### 5.3.3. Materials

Space-proven optical mirror technology is largely based on two approaches: open-back Schott Zerodur glass ceramic composite material and Corning ultra-low expansion ULE glass honeycomb structure. For SNAP either technology has sufficiently low coefficient of thermal expansion and sufficiently well proven manufacturing techniques. Studies are underway exploring the detailed fabrication and test flows using each process.

The metering structure will utilize a low-CTE carbon-fiber construction. In particular, the secondary support tripod will have to maintain the primary to



Fig. 11.— Cutaway view of the reference SNAP design. The entire telescope telescope attaches to the spacecraft structure by means of bipods. The outer baffle, shown cut away, also attaches to the spacecraft structure by means of its separate supporting struts. A discardable door, shown open in light gray, protects the cleanness of the optics until on-orbit commissioning begins. Solar panels are fixed, not deployed.

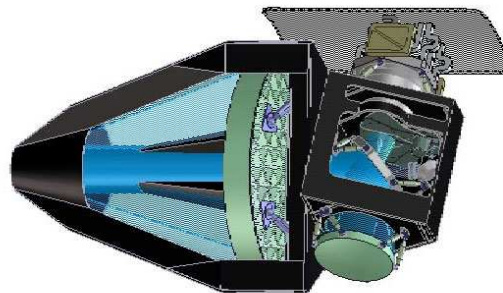


Fig. 12.— Telescope metering structure (carbon fiber, shown in dark gray) provides precision control of optical element spacings and orientations. Forward of the primary mirror, the secondary is supported on adjusters within the secondary baffle. Aft of the primary mirror, the tertiary metering structure supports the folding flat, the tertiary, and the focal plane instrumentation. The passive radiator at top is thermally but not structurally linked to the focal plane instrumentation.

TABLE 3  
OPTICAL SURFACES AND LOCATIONS

Optic	Diameter (m)	Central Hole (m)	Curvature ( $\text{m}^{-1}$ )	Asphericity	X Location, (m)	Z Location (m)
Primary	2.00	0.5	-0.2037466	-0.981128	0	0
Secondary	0.45	none	-0.9099607	-1.847493	0	-2.00
Folding flat	$0.80 \times 0.48$	$0.20 \times 0.12$	0	0	0	0.91
Tertiary	0.69	none	-0.7112388	-0.599000	-0.87	0.91
Focal plane	0.577	0.258	0	0	0.9	0.91

secondary spacing accurate to a few microns. This tripod, and the other major metering components, will certainly require a dedicated active thermal control system with passive cooling. We anticipate the need for five-axis motorized adjustment for the secondary mirror during ground integration, on-orbit observatory commissioning, and occasionally during science operations. For this reason we plan to include a hexapod or other multi-axis positioner into the secondary-mirror support structure.

The single highest priority bearing on the choice of mirror coating is the system throughput at the longest wavelengths where rest-frame optical photons from the highest-redshift supernova are the most distant and photons are the most precious. A secondary consideration is to establish a low thermal emissivity for the mirrors so that operating them at approximately 290K will not seriously impair our astronomical sensitivity in the NIR bands. The most common coating for astronomical mirrors at visible wavelengths is SiO overcoated aluminum. It offers outstanding durability and unmatched reflectance throughout the visible band, 0.4 to  $0.7 \mu\text{m}$ . A less common choice is protected silver, which is less efficient in the blue but more efficient in the red and NIR. The SNAP optical system has four reflections so its throughput varies as the fourth power of the mirror coating reflectivity. We have assumed here the use of protected silver rather than protected aluminum owing to its substantially higher total system throughput at the photon-starved wavelengths.

#### 5.3.4. Geometric-Optics Performance

In the reference SNAP optical configuration, the center of the focal plane is severely vignetted by the necessary hole in the folding flat which lies near the Cassegrain focus. In optimizing the optical perfor-

mance of the system, the useful imaging surface on the focal plane is taken to have an annular shape.

The optical performance of our reference telescope is fundamentally limited by aberrations and manufacturing errors at short wavelengths, and by diffraction at long wavelengths. Accordingly, our expected performance figures divide into two areas: geometrical ray traces that quantify the aberrations and pupil diffraction studies. We summarize the key performance items in Table 4 and Figure 13.

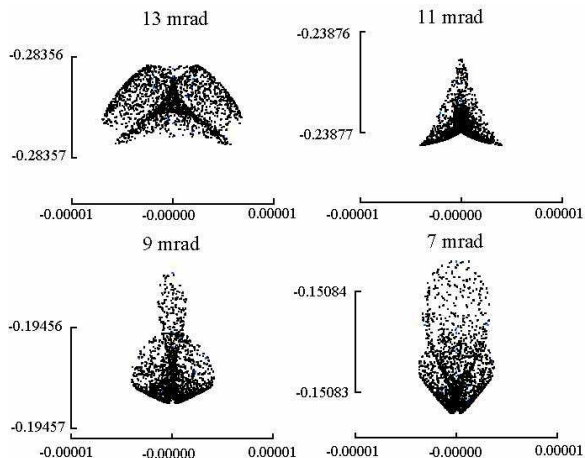


Fig. 13.— Ray trace spot diagrams. Upper left: 13 mrad off axis; upper right 11 mrad; lower left 9 mrad; lower right 7 mrad. Tick marks are spaced  $10 \mu\text{m}$  in the focal plane.

From spot diagrams at various off-axis angles, we have compiled the statistics on the mean radial centroid of ray hits in the focal plane, and the second moments of the spot distributions. These are listed in Table 5 in the form of the two orthogonal RMS breadths

TABLE 4  
REFERENCE OPTICAL PERFORMANCE

Parameter	Value/Performance
Focal Length	21.66 meters
Aperture	2.0 meters
Final focal ratio	f/10.83
Field	Annular, 6 to 13 mrad; 1.37 sq deg
RMS geometric blur	2.8 $\mu\text{m}$ , average 1 dimension
Central obstruction	16% area when fully baffled
Vane obstruction	4% area, tripod

(radial RMS and tangential RMS) in columns 2 and 3. The mean breadth is listed in column 4 below as microns on the focal plane, and in column 5 as an angular size on the sky in milliarcseconds. At the inner and outer radii of the image annulus, the FWHM becomes as large as 60 milliarcsec, although in the midrange of the annulus it is smaller.

Distortion is another fundamental optical aberration, but it does not impact the  $S/N$  nor does it directly impact the detection of supernovae unlike the other Seidel aberrations distortion. It does however cause the loci of scanned field objects to depart from parallel tracks in the focal plane, and does complicate the weak lensing science. In our reference design, we have disregarded distortion as a driver, in order to use all available design variables to maximize the working field of view and minimize the net geometrical blur. It is nonetheless important to explore the resulting distortion quantitatively. The telescope mirror assembly (TMA) distortion is axisymmetric owing to the symmetry of the unfolded (powered) optical train, and in polar coordinates any off-axis angle maps onto a single focal plane radius independent of azimuth angle. The distortion is therefore purely radial. Column 6 of Table 5 lists the radial distance of an off-axis field point as a function of the sine of the off-axis angle, and the departure from proportionality to the sine of that angle. The TMA distortion is of the pincushion type, having increased magnification toward the extremity of the field. Compared to a linear mapping of  $\sin \theta$  onto focal plane radius, the distortion amounts to about two percent.

### 5.3.5. Pupil Diffraction

For a star at infinity and a telescope focused at infinity, the pupil diffraction pattern is computed using the Fraunhofer formalism. The focal plane irradiance is simply the square of the modulus of the two-dimensional Fourier transform of the pupil. We have computed this irradiance function and diffracted light background for a variety of prospective metering structures.

### 5.3.6. Stray Light

A comprehensive stray light control plan has been developed for SNAP. The goal is to keep all stray light sources far below the natural zodiacal irradiance level as seen at the focal plane. The primary concern is sunlight scattered past the forward edge of the outer light baffle. This requires a minimum of two successive forward edges, since the light diffracted past a single edge would exceed the allowable irradiance at the primary mirror, assuming typical mirror scattering values. Figure 14 shows our treatment of the outer baffle interior vane arrangement. The mission reference L2 orbit simplifies the stray light design by eliminating the possibility of sun and full Earth light entering the main baffle from opposite directions. Analysis efforts are underway to quantify the effects of both out of band light rejected by the focal plane filters, as well as ghosting and internal reflections within the filters. A systems engineering approach is being pursued, along with development of a detailed stray light budget for both solar and stellar contamination sources.

TABLE 5  
OFF-AXIS ANGLE, IMAGE MOMENT, AND RADIAL DISTORTION

Off Axis $\sin \theta$	Radial RMS, ( $\mu\text{m}$ )	Tangential RMS ( $\mu\text{m}$ )	Average RMS ( $\mu\text{m}$ )	Average RMS (milliarcsec)	Radial Distortion ( $\mu\text{m}$ )
0.006	3.32	1.60	2.62	24.9	-838
0.007	3.33	1.60	2.62	24.9	-782
0.008	3.18	1.59	2.53	24.1	-630
0.009	2.83	1.51	2.28	21.7	-373
0.010	2.28	1.37	1.89	18.0	0
0.011	1.57	1.35	1.47	14.0	509
0.012	1.18	1.89	1.58	15.0	1165
0.013	2.09	3.23	2.73	26.0	1983
AVERAGE=			2.22	21.0	

### 5.3.7. Tolerances

The departure of any surface from its nominal mathematical conic section or the misplacement or misorientation of any of the surfaces causes a wavefront error and a degraded image quality. One measure of this degradation is the telescope’s Strehl ratio. The Strehl ratio can be converted into RMS wavefront error (RMS WFE) through Marechal’s relation. To achieve a system Strehl ratio of 0.77 at  $0.633 \mu\text{m}$  wavelength, the total WFE must not exceed 0.05 nm RMS. This allowed WFE will be apportioned into individual contributions as part of the detailed telescope design.

A tolerance budget has been developed based on a group of exploratory studies of the sensitivity of the geometrical spot size to variations in element curvature, shape, location, and orientation. These calculations show that by far the single most critical parameters are the primary mirror curvature and the spacing between primary and secondary mirrors expected given the fast ( $f/1.2$ ) primary mirror. A two-micron displacement of the secondary piston, or a two-micron displacement in the virtual image created by the primary mirror is found to increase the RMS geometrical blur by about  $3 \mu\text{m}$ . Similarly, a  $15\text{-}\mu\text{m}$  lateral displacement or a  $15\text{-microradian}$  tilt of the secondary mirror causes a  $3\text{-}\mu\text{m}$  growth in the RMS geometrical blur.

The reference model SNAP telescope includes on-orbit mechanical adjustments that permit the relocation and reorientation of the secondary mirror, and possibly the tertiary mirror as well, to optimize image

quality. By means of these adjustments we anticipate accommodating small shifts in any of the optical elements locations and orientations, allowing for correction of geometrical blur.

### 5.4. Imager

The wide field of view of the SNAP imager allows simultaneous batch discovery and building of supernova rest-frame optical light curves, and over the mission lifetime will yield several thousands of supernovae at  $0.1 < z < 1.7$  with the proposed photometric accuracy. More distant, less precisely measured supernovae will also be available in our data set. The multiplexing advantage with this large field reduces by more than an order of magnitude the total exposure times necessary to follow all the supernovae. Figure 3 shows critical points on the light curve and the desired measurement accuracy that the SNAP imager must furnish. We note that the stated  $S/N$  need not be achieved with a single measurement but can be synthesized from multiple measurements, taking advantage of the substantial time dilation for high-redshift supernovae.

Weak lensing by large-scale structure is a statistical study that requires the accurate measurement of the shapes of many galaxies. In order to efficiently survey a large area in a finite time, a large field of view covered by detectors with high quantum efficiency is necessary. Given a fixed number of pixels in the focal plane, there are competing desires to have better resolution, which requires smaller pixel scales and wider sky coverage, which requires larger pixel



Fig. 14.— Schematic treatment of the outer baffle interior vane arrangement. Sunlight is incident from the left, where the height of the baffle and its angled forward edge maintains the baffle interior in darkness.

scales. The theoretical optimum of this trade-off requires that the pixel size be roughly matched to the size of the PSF (Bernstein 2002); further plate scale and pixel size studies using both simulated and real data are currently in progress for optimizing photometric and shape-measurement accuracy while maintaining a large field of view. For the case of the state-of-the-art SNAP CCDs in which the PSF size is dominated by diffusion in the silicon at  $\sim 8000 \text{ \AA}$ , the theoretical optimum requires a pixel size of roughly 0.1 arcsecond. (Diffusion would be worse in a conventional CCD that has a field-free region.) In order to make precise, bias-free photometric redshift measurements, wide spectral coverage for the optical to near infrared is needed. Such photo- $z$  measurements are crucial to interpreting the cosmological implications of the wide-field survey. The aforementioned capabilities are necessary to measure the shapes of a significant number of faint galaxies beyond  $z = 1$  in order to study the evolution of structure. Crucially important systematic errors in shape measurements arising from unstable anisotropic PSFs and systematic errors/biases in photometric redshift determination are significantly reduced in a space-based imager such as SNAP when compared to ground-based facilities.

The SNAP imager addresses the above requirements using two detector technologies to efficiently cover the wavelength range of  $3500 \text{ \AA}$  to  $17000 \text{ \AA}$ . The visible region ( $3500 \text{ \AA}$  to  $10000 \text{ \AA}$ ) is measured with Lawrence Berkeley National Laboratory new-technology  $p$ -channel high-resistivity CCDs (Holland et al. 2003; Stover et al. 2000; Groom et al. 2000) which have high ( $\sim 80\%$ ) quantum efficiency for wavelengths between  $3500$  and  $10000 \text{ \AA}$ . Extensive radiation testing shows that these CCDs will suffer little or no performance degradation over the lifetime of SNAP (Bebek et al. 2002a,b). In the reference design a pixel size of  $10.5 \mu\text{m}$  has been matched to the telescope focal length and diffraction limit at  $10000 \text{ \AA}$  of 0.1 arcsec. Improved shape measurements and robust PSF photometry come from a dithered observation strategy. Undersampling, dithering, cosmic ray hits, and many other effects are included in the exposure time calculator developed by Bernstein (2002).

The NIR range ( $9000 \text{ \AA}$  to  $17000 \text{ \AA}$ ) is measured with commercially available HgCdTe arrays. Current large area ( $2048 \times 2048$  pixel) HgCdTe detector devices have a pixel sizes in the range of  $18 - 20 \mu\text{m}$ . The telescope optics are designed to give an angular pixel size of 0.17 arcsec, matched to the telescope fo-

cal length and diffraction limit at 17000 Å. The SNAP reference performance specifications require low read noise and dark current ( $< 6\text{-}8 e^-$  for multiple reads and  $< 0.1 e^-/\text{sec}/\text{pix}$ , respectively), high quantum efficiency ( $>60\%$ ), and uniform pixel response. Reference imager detector specifications are given in Table 6. The evolution of the SNAP focal-plane design is described in Lampton et al. (2002a).

The minimum filter set required is primarily determined by the precision needed for the cross-filter  $K$ -correction, that is necessary when reconstructing the primary restframe band ( $B$ -band in the reference design) light from a set of laboratory-frame filter measurements. Six visible filters and three NIR filters are sufficient if they are derived from a  $B$ -band filter with logarithmic  $(1+z)$  scaling of their wavelength centers and widths. The reference set that we consider here consists of nine redshifted  $B$  filters logarithmically distributed in wavelength with effective wavelengths at  $4400 \times 1.15^n \text{Å}$  for  $n \in \{0, 1, \dots, 8\}$ . Further optimization of the filter set for supernova science and photometric-redshifts is in progress. In particular, the ultimate SNAP “ $B$ ” filter will not necessarily be a Johnson  $B$  although it is expected to have a similar central wavelength and width.

A fixed-filter design is preferred over a large filter wheel which would be a single point failure risk. Figure 15 shows an array of visible and NIR filters in the SNAP focal plane. To enhance the amount of NIR light that is integrated, the individual NIR filters have twice the area in the focal plane of the individual visible filters. The constraint that the satellite be rotated in  $90^\circ$  increments requires the filter pattern to remain symmetric with respect to two orthogonal axes. Consider the filter arrays in Figure 15. Note that the arrays can be scanned through an observation field left-to-right, right-to-left, top-to-bottom, and bottom-to-top, and that a given star will be measured with each filter bandpass but not necessarily the same physical filter. Note that any  $90^\circ$  rotation of the filter array can still measure the star field in all filter types.

As shown in Figure 15, underlying each NIR filter is one  $2k \times 2k$ ,  $18 \mu\text{m}$  HgCdTe device, 36 in total. Underlying each  $2 \times 2$  array of visible filters is one  $3.5k \times 3.5k$ ,  $10.5 \mu\text{m}$  CCD, with 36 devices in all. The total number of pixels is  $\sim 600$  million.

The SNAP focal plane will be passively cooled to operate at 140K, a habitable temperature for the CCDs and sufficiently cold to achieve the noise requirements from the  $1.7 \mu\text{m}$ -cutoff HgCdTe devices. Short flex ca-

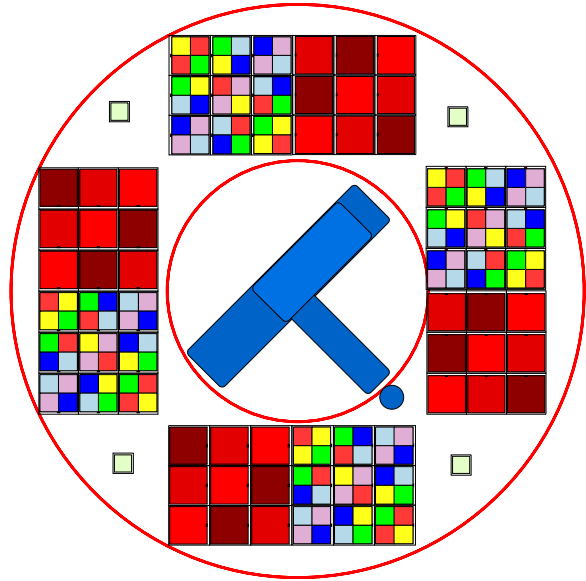


Fig. 15.— The SNAP focal plane working concept. The two-axis symmetry of the imager filters allows any  $90^\circ$  rotation to scan a fixed strip of the sky and measure all objects in all nine filter types. The imager covers 0.7 square degrees. Underlying the filters, there are 36  $2k \times 2k$  HgCdTe NIR devices and 36  $3.5k \times 3.5k$  CCDs on a 140K cooled focal plane. The six CCD filter types and three NIR filters are arranged so that vertical or horizontal scans of the array through an observation field will measure all objects in all filters. The false colors indicate filters with the same bandpass. The central rectangle and solid circle are the spectrograph body and its light access port, respectively. The spectrum of a supernova is taken by placing the star in the spectrograph port by steering the satellite. The four small, isolated squares are the star guider CCDs. The inner and outer radii are 129 and 284 mm, respectively.

TABLE 6  
REFERENCE MISSION SPECIFICATIONS FOR THE IMAGER AND ITS SENSORS

Parameter	Visible	NIR
Field of View (deg <sup>2</sup> )	0.34	0.34
Plate scale (arcsec)	0.10	0.17
Wavelength (Å)	3500–10000	9000 – 17000
⟨Quantum efficiency⟩ (%)	80	60
Read noise (multiple reads) (e <sup>-</sup> /pixel)	4	6–8 (multiple read)
Dark current (e <sup>-</sup> /s/pixel)	0.002	0.1
Diffusion (μm)	4	5
Number of fixed filters	6	3

bles penetrate the focal plane to bring the signals to the electronics located on the backside. The present reference design envisions an ASIC-based readout that would also operate at 140K; this avoids routing low-level analog signals long distances and reduces the size of the cable plant between the cold focal plane and the warm data acquisition electronics located to the side.

A four-channel custom chip will read out each CCD (Walder et al. 2003). It consists of a single-ended to differential converter followed by a correlated double sampler and a novel multi-slope integrator. This circuit is designed to operate at room temperature for test purposes and at 140 K. The readout speed is 100 kHz. The 16-bit dynamic range is covered using 3 gains each with a 12 bit signal to noise ratio. A 12-bit pipeline ADC digitizes the analog data.

In the deep survey, multi-band exposures of a point of sky will be achieved by shift-and-stare observations in which the pointings are shifted by the 2.9 arcmin width of the optical filters. Each pointing will consist of four 300-second exposures; the multiple exposures are for cosmic-ray rejection and dithering of our under-sampled pixels. The fixed filters prevent independent tuning of exposure times for different filters. Within a scan, over one hundred pointings are required to cover the 7.5 square degrees in all filters to the desired depth. A scan of the north (south) field will be repeated every four days for 16 months for a total 120 scans.

In the wide (and panoramic) surveys, long adjacent strips will be observed using the shift and stare method. Six rather than four dithers will be made per pointing so as to fill the gaps between the detectors and provide robust galaxy-shape measurements. Observed patches of sky will not be revisited. The exact shapes

of the fields are under review.

### 5.5. Spectrograph

The spectrometer is used to make a positive identification of Type Ia supernovae by observing the characteristic SiII feature at 6150Å, measure the features associated with supernova heterogeneity, determine the redshift of the underlying host galaxies and supernovae, build a template spectral library of SNe Ia, and link standard stars with the SNAP photometric system.

The specific signature of Type Ia supernovae is the SiII line at  $\lambda = 6150\text{\AA}$  (rest frame). In models, the strongest sensitivity to the metallicity in the progenitor system lies in the rest-frame UV band. The need for both supernova-frame UV and Si features defines a broad wavelength range, 4000 - 17000 Å that must be covered by the instrument to observe  $z \leq 1.7$  supernovae. The broad features of the supernova spectra and the non-negligible detector noise contribution for the faintest objects make a low-resolution spectrograph optimal: studies (Bernstein & Kim 2004) find an optimal resolving power  $\lambda/\delta\lambda \sim 100$  at FWHM and 1 pixel per FWHM sampling, with constant resolving power in the 0.6-1.7μm range. Other types of supernovae, such as II or Ib, have lines of H or He in the same wavelength range with similar equivalent widths, allowing supernova classification of all possible candidates with one spectrograph.

The silicon feature and other features in the spectrum of a typical Type Ia supernovae, shown in Figure 4, are to be carefully observed. Their characteristics (position, width, height, etc.) are related to the supernova peak magnitude through physical parameters such as temperature, velocity and progenitor metallic-

ity.

The field of view must include the underlying galaxy in order to determine its spectrum during the same exposure. This is necessary for subtraction of the host spectrum from the spectrum in the supernovae region, and for an accurate determination of supernova redshift. To avoid single-point failure in the spectrograph we desire two detectors in each focal plane. The detectors cover  $3'' \times 6''$  split into 40 slices that can easily cover the mean size of galaxies at redshift 1-2. The large field of view allows the pointing requirements to be relaxed. The main spectrograph specifications are summarized in Table 7. See Ealet et al. (2003) for details on the design process.

### 5.5.1. Integral Field Unit

The requirement for simultaneous acquisition of supernova and host spectra, the ability to subtract off the host-galaxy spectrum after the supernova has faded, spectrophotometry for calibration purposes, and the high object acquisition precision that would be needed for a traditional long slit spectrograph, make a 3D spectrograph an attractive option. A 3D spectrograph reconstructs the data cube consisting of the two spatial directions X and Y plus the wavelength direction. For each spatial pixel, the spectrum is reconstructed. Two principal techniques are indicated for 3D spectroscopy: first, the use of a Fourier Transform Spectrometer (FTS), and second, the use of integral field spectroscopy.

Trade studies indicate that integral-field spectroscopy using the image slicer technique is preferred for SNAP. This technique, developed since 1938 in order to minimize slit losses, is very powerful (Bowen 1938; Content 1997; Prieto et al. 2002). The new generation of image slicers improves the efficiency and the compactness of the system and appears to be a very well adapted solution for the SNAP mission.

Figure 16 shows the principle of this technique. The field of view is sliced along  $N$  (in the drawing  $N = 3$ , for SNAP  $N = 40$ ) strips on a slicing mirror, consisting of a stack of  $N$  plates where the active surface is on an edge. Each of the  $N$  slices re-images the telescope pupil, creating  $N$  telescope pupil images in the pupil plane. Thanks to a tilt adapted to each individual slice, the  $N$  pupil images lie along a line. In the pupil plane, a line of “pupil mirrors” is arranged. Each pupil mirror is placed on a pupil image and reimages the field strip. These images are arranged along a line

and form a “pseudo-slit”. At this stage, therefore, there is an image of each of the  $N$  strips of the field of view. The pseudo-slit is placed in the entrance plane of the spectrograph, acting as the entrance slit. A last line of mirrors is placed on the pseudo-slit. This line adapts the output pupil of the slicer into the input pupil of the spectrograph.

### 5.5.2. Reference Spectrograph Instrument Concept

The spectrograph components are summarized in the block diagram shown in Figure 17 with the principal components described below.

#### Relay Optics

This unit is the interface between the telescope beam and the instrument. Some telescope aberrations can be corrected within this optical system. A simple three-mirror configuration should be sufficient to allow pick-

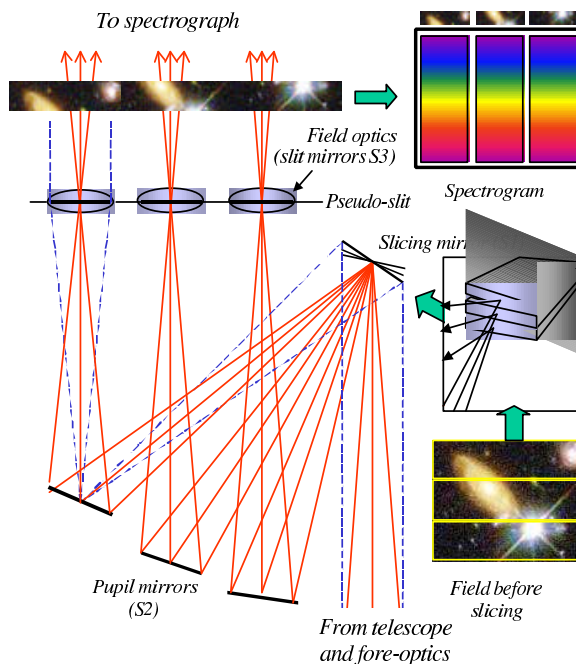


Fig. 16.— Principle of the image slicer. The field of view is sliced along  $N$  (here  $N = 3$ ) strips on a slicing mirror. Each slice re-images the telescope pupil onto a line of “pupil mirrors” which reimages the field strip along a “pseudo-slit”. The pseudo-slit is placed in the entrance plane of the spectrograph, acting as the entrance slit (courtesy J. Allington-Smith, Durham U.).

TABLE 7  
REFERENCE MISSION SPECTROGRAPH SPECIFICATIONS

Property	Visible	NIR
Wavelength coverage ( $\mu\text{m}$ )	0.35-0.98	0.98-1.70
Field of view	$3.0'' \times 6.0''$	$3.0'' \times 6.0''$
Spatial resolution element (arcsec)	0.15	0.15
Number of slices	40	40
Spectral resolution, $\lambda/\delta\lambda$	100	100

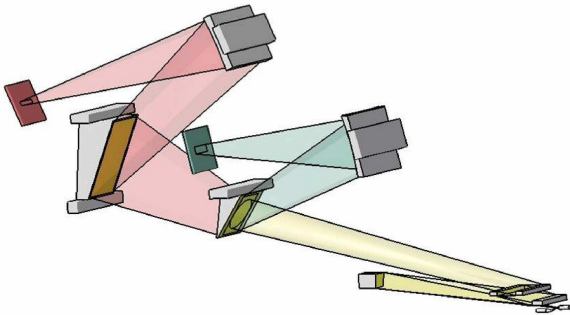


Fig. 17.— A schematic spectrograph optical design. The beam is going out from the slicer (on the bottom right) to a prism disperser back faced coated by a dichroic. The visible light (blue path) is reflected and the IR light (in red) continue to a second prism used to reach the required spectral dispersion. The two beams are therefore focused on two detectors. The dimensions of the spectrograph are approximately  $400 \times 80 \times 100$  mm.

ing off the beam at a point most convenient for the spectrometer.

#### *Slicer Unit*

The slicer unit acts as a field reformatting system. As described above, the principle is to slice a 2D field of view into long strips and optically align all the strips to form a long spectrograph entrance slit. The slicing mirror is comprised of a stack of slicers. Each slicer has an optically active spherical surface on one edge. A line of pupil mirrors does the reformatting. Each pupil mirror sends the beam to a slit mirror, which adapts the pupil to the entrance of the spectrograph.

The long thin active surface of each individual

slicer will produce a large diffraction effect. In order to minimize flux losses to a few percent, the spectrograph entrance pupil must be oversized. A combined theoretical and experimental approach is underway at Laboratoire d'Astrophysique de Marseille to define the optimum entrance pupil for a JWST application (in the infrared bands 1-5  $\mu\text{m}$ ). This will be directly adapted for the SNAP concept.

The reference requirements on the slicer unit are an accuracy of  $\leq \lambda/10$  RMS on the optical surfaces and a surface roughness of  $\leq 50$  Å RMS. Existing prototypes fully meet these specifications.

#### *Optical Bench*

Thanks to the moderate beam aperture and field of view, the spectrograph optics will be straightforward. The reference is a classical dichroic spectrograph: one collimator mirror, one prism with a dichroic crystal, and two camera mirrors are required. Using spherical shapes for all the mirrors would provide an adequately sharp image, but using aspheric mirrors will make it possible to have a very compact spectrograph. The prism solution is well matched to the requirement of a constant resolution over the whole wavelength range. The dichroic crystal allows the coverage of two channels simultaneously: one for the visible (e.g.. 0.35–0.98  $\mu\text{m}$ ) and one for the infrared (0.98–1.70  $\mu\text{m}$ ).

#### *Detectors*

In the visible, the main goals are high quantum efficiency and very low noise. Given concerns over degradation due to radiation exposure and the poor performance of conventional thinned CCDs in the red part of the visible, the fully-depleted LBNL CCDs are the detectors of choice. Thinned, back-side illuminated, deep depletion, low-noise conventional CCDs of 1024

$\times 1024$  pixels are an alternative option. In the NIR, some factors constrain the detector technologies. The operating temperature will be dictated by the detector dark current. HgCdTe arrays with cutoff wavelength of  $1.7 \mu\text{m}$  are currently under consideration which allow operation in the 130-140 K range. A detailed list of the performance specifications for the detectors is provided in Table 8. To achieve the listed performance in read noise and dark current, a multiple sampling technique is required. To optimize exposure time, the impact of the rate of cosmic rays on the spectrum quality is under study.

### 5.5.3. Efficiency Estimate

Simulations of the efficiency of the instrument show a cumulative efficiency of the instrument from the relay optic and including the detector at a level better than 50% in the visible and 40% in the infrared. This excellent performance is due to high slicer efficiency and is based on a conservative value for the efficiency of individual mirrors (98%), much lower than is expected from a silver coating at these wavelengths. The principal losses are from the prism (also conservatively estimated at 80%), and from the detector.

## 5.6. Telemetry

During the reference deep survey, the observation time of SNAP is partitioned roughly 60% to preprogrammed, stepped photometry and 40% to targeted spectroscopy with parallel photometry. The former is divided into a sequence of 300s exposures followed by 30s of sensor readout. The latter is comprised of exposures varying from a few seconds to a thousand seconds. For the longer exposure times, the spectrograph NIR detector is continuously read in up-the-ramp mode to allow cosmic-ray rejection. Imaging is possible during spectroscopic exposures; the imager is read as in photometry mode except that the exposure times vary, determined by the time to achieve a required  $S/N$  in the spectrograph for a particular supernova. For each imaging exposure, the CCD devices produce a single frame of correlated double sampled data while the NIR devices produce two frames (each containing the average of multiple reads), one for post reset values and the other for post integration values so that the digital correlated double sampling can be done on the ground.

The operating concept for processing the raw data

is to perform only lossless compression of the frames in the satellite. A factor of two is easily done; a greater compression factor is probably achievable. The primary motivations are to be able to look retrospectively into the data to better determine a supernova explosion time and to be able to co-add many months of data for weak lensing science to extract weak signals from the per frame noise. With this approach we avoid developing flight software for automated acquisition and processing of reference, dark and flat frames and applying them irrecoverably to data frames. The consequence is that in L2 SNAP will require about 133 Gb of flight data storage for a 24 hour contact period through the Deep Space Network capacity. We anticipate that DSN will have the ability to receive  $300 \text{ Mbit s}^{-1}$  Ka-band data by the time SNAP launches.

The current reference weak lensing survey (Rhodes et al. 2004) calls for a 1-year 1000 square degree survey consisting entirely of imaging. At L2, 6 dithered exposures per optical filter would be taken for a total of 1900 s. Such a survey would require a daily four hour download of data and would use only  $\sim 150$  GB of on-board storage. A wider survey could be taken if more time were given to the survey or if the exposure time per filter were lowered. The latter option would require that the data download time be accordingly raised to compensate for more exposures or that the on-board compression of the data be increased beyond the factor of two that can be achieved through lossless compression.

## 6. Calibration Program

An important feature of the supernova-cosmology analysis is its dependence on the *relative* brightness of Type Ia supernovae. Cosmological and dark-energy parameters are determined from the shape, and not the absolute normalization, of the Hubble brightness-redshift relationship. In order to constrain the possible effects of population evolution, SNAP will use homogeneous subsets of SN Ia. Identification of these SN Ia subsets depends in part on the brightness and color evolution of supernovae. Each supernova redshift  $z$  is plotted against its restframe B band flux which depends on the K-correction and the extinction correction, which in turn depend on the color of the supernovae. As a result, the analysis relies on the *color*, where we use this term to mean the flux ratios of calibrated passbands. The SNAP calibration program must thus precisely control the absolute *color* calibra-

TABLE 8  
REFERENCE MISSION SPECTROGRAPH DETECTOR SPECIFICATIONS

	Visible	NIR
Detector size	1k × 1k	1k × 1k
Pixel size ( $\mu\text{m}$ )	10-20	18-20
Detector temperature(K)	140	130-140
$\langle\text{QE}\rangle(\%)$	>80	>60
Read noise( $\text{e}^-/\text{pixel}$ )	2	5 (multiple read)
Dark current( $\text{e}^-/\text{pixel}/\text{s}$ )	0.001	0.02

tion, not necessarily the absolute flux calibration, in the  $0.35 - 1.7 \mu\text{m}$  observing window.

The SNAP calibration program will provide fluxes in physical units associated with the same restframe passband for a homogeneous set of supernovae distributed out to  $z = 1.7$ . Calibration provides the transformation of the measured signal in a given passband into a flux associated with a calibrated passband. Calibration affects flux-correction for extinction due to the Milky Way, the SN host galaxy, and the intergalactic medium, and also the K-corrections which provide the transformation between fluxes in the observed and restframe passbands.

In the SNAP cosmological-parameter determination, calibration enters early in the analysis and consequently the calibration uncertainty propagates non-trivially throughout. Depending on its nature and size, the calibration uncertainty can contribute significantly to the  $w_0 - w'$  error budget. The propagation of these uncertainties has been explored in Kim et al. (2004) for a simplified blackbody calibration model. Realistic calibration uncertainty will be more complex and the SNAP calibration methodology is being crafted to ensure that calibration does not impede achievement of the science goals.

The SNAP reference calibration concept consists of several programs which are subject to ongoing work examining modifications, extensions, and alternative strategies. A set of astronomical sources with known physical fluxes (or more importantly known physical colors) are established as “fundamental standards”. A network of fainter primary and secondary standard stars, accessible to SNAP and larger ground-based telescopes, are established with respect to the fundamental standards. The SNAP observatory has an observation and analysis program that takes standard

star observations and derives a transformation between SNAP signals and fluxes in the instrument passbands. These programs are described in detail in the following subsections.

### 6.1. Fundamental Standards

In the ideal situation, target supernovae would be calibrated directly against a true irradiance standard observed through the same optical chain. However, because of the unavailability of convenient irradiance standards observable through the same optical path as the supernovae, a suitable, calibrated proxy (or proxies) must be identified. Consequently SNAP must use stars as irradiance and color standards (standard candles). These selected stars may be established as standards using calculations of model stellar atmospheres as a substitute for a NIST-traceable irradiance standard. A few stars may be unreddened and easy to model, so that all or part of the standard candle flux distributions can be replaced by a suitably normalized model atmosphere calculation. Traditionally in optical astronomy the bright,  $V = 0$  star Vega has been used as the NIST stand-in. However, Vega itself is far too bright to be used for most astronomical programs, so it has been used to calibrate fainter stars e.g. the Landolt standards, Oke standards etc. The SNAP calibration program has identified “fundamental standard stars” to be bright,  $V \sim 12$ , stars whose spectral energy distributions are independently determined. At  $V = 12 - 13$ , the fundamental stars may be observed with the SNAP spectrograph.

The current Hubble Space Telescope fundamental flux standards are a set of three WD stars and could be a good choice for the basis of the SNAP flux calibration. These stars have pure hydrogen atmospheres and are too hot for molecular constituents, which means

that the physics of the model calculations are relatively straightforward. The three models are normalized near 5500 Å using Landolt V band magnitudes. The HST program (Bohlin et al. 2001) also provides three primary solar analog standards, whose optical flux has been measured on the WD flux scale and whose IR flux shape is solar. The stellar model approach is a tested method that yields a precision of  $\sim 1\%$  in the UV and optical, while the near infrared relative fluxes are less well tested. The systematic flux errors in the WD model technique have been estimated by the difference between the two extreme models that still fit the observations. This uncertainty reaches a maximum in the SNAP wavelength range of 1.8% at  $1.7\mu\text{m}$ , meeting the goals of the reference mission. One possibility for further reducing the uncertainties is to verify that the WD model  $T_{eff}$  and  $\log g$  values derived from the Balmer line profiles fit uniformly for the Lyman and Paschen lines, as well. A second verification in progress with NICMOS is to confirm to  $< 1\%$  the relative IR fluxes of the models and the solar analogs.

The direct method of determining stellar fluxes is to compare observations of stars, particularly in the near infrared, with a lamp source. As stated in Bohlin et al. (2001) “In order to improve the accuracy of the standard star IR flux distributions, some standard stars should be compared to an actual standard IR lamp to define a proper absolute flux calibration, just as was done for Vega. . . such fundamental data are lacking . . .” These authors normalize the flux scale at one bandpass once the spectral shape has been determined, while a lamp comparison determines both the absolute level and the shape of the spectral flux distribution. The absolute calibration of Vega (Hayes & Latham 1975; Hayes 1985) exemplifies a direct method of establishing a fundamental calibrator. The need and approach for such an experiment is under study by the SNAP calibration team.

## 6.2. SNAP Standard Star Network

In order to minimize the need for on-orbit calibration time, a ground-based standard star network consisting of the fundamental standards linked to primary and secondary standards will be established. This network will provide the preliminary calibration data for the spacecraft by setting the spectrophotometric zero-points. Further, the network will enable parallel and follow-on observation from the ground to support on-orbit science observations. The network will establish an all-sky photometric system covering the spectrum

from 3500 to 17000 Å and spanning approximately 6 magnitudes (12 to 18 mag) of brightness.

Primary standards are fainter ( $V = 15 - 18$ ) than the fundamental standards and will be calibrated with respect to the fundamental standards through spectrophotometry and photometry. They will be used to transfer the calibration to an “all sky” grid. Some will lie in the SNAP science fields and others around the celestial equator to tie the northern and southern SNAP fields together and provide standards distributed over 24 hours. The primary standards will be tied to the secondary standards through spectrophotometry and photometry. Secondary standards will be in the SNAP fields. They will span a wide color and magnitude ( $V > 18$ ) range, and hence spectral type. Uncertainties will be minimized by multiple observations of the fields.

Once in orbit, we will verify the zero-points for both the primary and the secondary standard stars. The planned repeating observation cadences will allow typically 140 observations of every star in the SNAP-N and SNAP-S fields over the course of the mission, leading to refinement of the brighter secondaries and establishment and verification of the fainter secondaries.

## 6.3. Calibration Transfer

SNAP is developing a flux-based (rather than magnitude-based) plan for transferring the fundamental standard star calibration to the primary and secondary standards, and ultimately to supernovae through a combination of spectroscopy and photometry. There are two common choices of calibration passbands. Traditionally in observational astronomy a set of passbands is associated with a specific magnitude system. These (virtual) passbands, when used to observe the system’s primary standard stars, reproduce exactly the tabulated magnitudes. Bessell (1990) has produced throughput realizations of the Johnson-Cousins magnitude system. Another approach is to use observations to infer the actual throughput of the observers optical system (including atmosphere). SNAP can use both approaches in its calibrations. Further, as the demand for precise calibration is fairly stringent, SNAP needs to be able to account for changes in the instrument performance. For example, we intend to re-determine the transmission properties of the photometry filters during the mission by taking advantage of the multiple observations of stars in the SNAP

fields provided by the 4-day observing cadence. Internal calibrated, stable illumination sources may also be utilized.

## 7. SNAP Simulation

The design of the SNAP reference mission has been guided by the Fisher-matrix analysis described in §2.3. A detailed simulation of the reference mission now provides validation of the scientific reach of the SNAP mission and provides a tool for further mission refinement and optimization. We have developed a detailed parameterized simulator of supernova cosmology missions. We describe here its use in projecting the scientific yield from the SNAP supernova reference mission described in this paper. A similar but more complete pixel-level simulation will be used to test the mission-analysis software.

For the telescope/camera configuration and observing plan described in the previous sections, we generate a list of Type Ia supernovae and their associated host galaxies in the observed field of view during the course of the survey. The incident flux at the telescope is calculated for each supernova, accounting for the underlying cosmology, magnification from gravitational lensing, and host and Galactic dust. The photometric observations of the supernovae from the SNAP scanning strategy are simulated, resulting in multi-band light curves for each event.

The rest-frame  $B$  and  $V$  light curves are fit to SN Ia-class templates while the light curves in other filters are fit to a polynomial, in order to measure the magnitude, color, and light-curve parameters of each supernova. Triggered spectroscopic observations are simulated through Fisher-matrix techniques (Bernstein & Kim 2004) which predict the quality of the spectroscopic parameter measurements. Supernova observables are related to the intrinsic peak absolute magnitude using the models described in Höflich et al. (2003). In this manner, supernova’s light-curve and spectral parameters are then used to determine its distance modulus, along with host-galaxy extinction ( $A_V$  and  $R_V$  of the Cardelli et al. (1989) dust model) and its individual absolute magnitude.

Given the reference SNAP supernova distribution and expected distance moduli folded with the expected supernovae from the Nearby Supernova Factory, we fit the cosmological parameters. While this can be done for a general set of parameters, we concentrate on the dark-energy parameters  $w_0$  and  $w'$  assuming a flat uni-

verse and a fiducial model with  $w_0 = -1$  and  $w' = 0$  (recall we define  $w' \equiv dw/d \ln a|_{z=1} \approx w_a/2$ ). The standard systematic-error model is adopted. Marginalizing over all other parameters, we get uncertainties in  $w_0$  of 0.07 and  $w'$  of  $\sim 0.31$  for the prior 0.03 uncertainty in  $\Omega_M$ . If we take no prior in  $\Omega_M$  but assume cosmological constraints expected from Planck, the  $w'$  uncertainty improves to  $\sim 0.16$ . These results are somewhat better than those determined in the Fisher analysis shown in Table 1 where all supernovae are assumed to have identical distance-modulus uncertainty. By setting exposure times based on light-curve requirements for the highest redshift supernovae, the lower redshift events have better  $S/N$  with the fixed filter design.

To explore how SNAP will be able to distinguish between different dark-energy models, we simulate constraints on  $w_0$  and  $w'$  choosing as fiducial models instantiations of two postulated theories that account for an accelerating universe: a cosmological constant and a supergravity-inspired model. Using Monte Carlo we generate 68% confidence contours for SNAP supernovae, in conjunction with the data anticipated from the Planck mission, and SNAP supernovae and weak lensing. (Figure 18). We marginalize over the absolute magnitude and  $\Omega_M$  with no prior imposed on either.

Even with just SNAP supernovae, the chosen models are distinct, with the fiducial values lying well outside the 68% contours of the other model. Inclusion of SNAP weak-lensing power spectrum, bispectrum, and cross-correlation cosmography information provides improved sensitivity. SNAP and complementary data will provide important guidance to the true nature of dark energy.

We have done the most detailed simulation of a weak lensing survey to date by identifying instrumental aspects of SNAP that will affect the PSF, applying this PSF to simulated images, and calculating the lensing efficiency and subsequent constraints on cosmological parameters from the SNAP weak lensing survey. The results of these studies are in Rhodes et al. (2004); Massey et al. (2004); Refregier et al. (2004). The cosmological reach of the SNAP weak-lensing program presented in this paper is based on these simulations. We are continuing to develop the image simulations for more accurate results and to better identify instrumental factors that might be tweaked for gains in sensitivity to weak lensing. We also are exploring the impact of new analysis techniques, e.g. bispectrum measurements of the mass distribution and

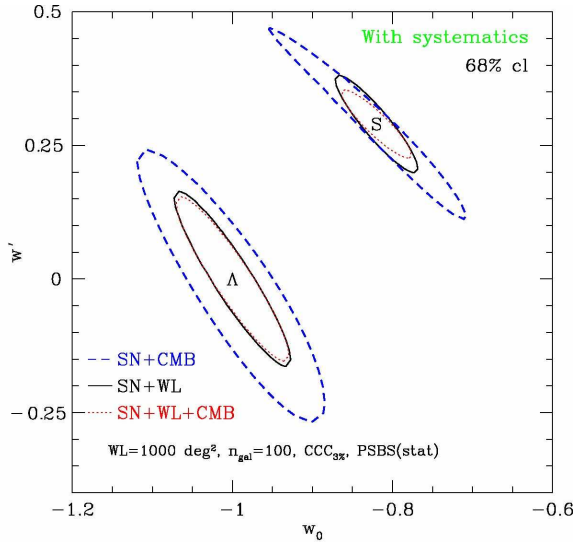


Fig. 18.— The 68% confidence region in the dark-energy parameters for fiducial cosmological constant (labeled with  $\Lambda$ ) and supergravity (labeled with S) universes. The blue dashed curves show the results of the supernova simulation with a Planck prior and an assumed flat universe. Using Fisher analysis, we find significant improvement is obtained using the SNAP supernova and 1000 square-degree weak lensing surveys (black curves). Additional CMB data (dotted red curves) provides additional constraints for the supergravity universe, but not for the fiducial cosmological model. We define  $w' \equiv dw/d \ln a|_{z=1}$ .

cross-correlation cosmography, for measuring dark-energy parameters (Bernstein & Jain 2004; Jain & Taylor 2003; Takada & Jain 2003).

## 8. Ancillary Science with the SNAP Survey Fields

The SNAP surveys will have an unprecedented combination of depth, solid-angle, angular resolution, temporal sampling, and wavelength coverage from the optical to the NIR. The wealth of potential science from deep and wide-field surveys has already been demonstrated in such surveys as the Hubble Deep Fields (Williams et al. 1996, 2000) and the SDSS (Abazajian et al. 2003). In §4 we summarized how the SNAP data set will contribute to our understanding of dark energy. We here explore the properties of the surveys and their potential scientific yield in other areas.

### 8.1. SNAP Survey Depth

Based on the telescope and camera characteristics, we quantify the expected depth, solid-angle, and time resolution of the SNAP supernova and weak lensing surveys. The telescope and camera properties of SNAP have been modeled and incorporated into an advanced exposure-time calculator (ETC) (Bernstein 2002). Besides having all the usual capabilities of a standard ETC, our ETC includes unique handling of the pixel response function, undersampling, dithering, and probabilistic cosmic-ray rejection. As mentioned in §5.4, SNAP will use dithering to obtain spatial resolution below the pixel scales.

The high cosmic-ray flux in a space environment produces a non-trivial reduction of effective exposure times; pixels from a single exposure that are contaminated by a cosmic ray are recognized through median and other filtering and dropped in the dithered reconstruction. The expected contamination probability of a point source is 0.0002 per second. Short individual exposure (plus readout) times limit the contamination: four 300 second exposures give better than a 99% probability that there will be no cosmic-ray contamination at a given position for at least one of the dithers that make up a pointing.

The magnitude depths for individual scans and co-added images of the SNAP supernova fields are calculated for each filter. Table 9 shows the limiting  $S/N = 5$  AB magnitude for each filter in the surveys, for point sources that are not contaminated with cosmic rays. As with the HST, the limiting magnitude for any given point is probabilistic, due to the random occurrence of cosmic rays. The probability for a given level of cosmic contamination (and approximate degradation in signal-to-noise) can be determined using the binomial distribution. In a single scan of the deep survey 77% of point sources will have no cosmic contamination in any of the four dithered images while 98% will have one or fewer cosmic-contaminated image, only slightly reducing signal-to-noise.

The SNAP observing strategy provides remarkably even depth over the range of filters. For a given filter, *individual scans* of the deep and wide-field surveys are only  $\sim 0.75$  magnitudes shallower than the Hubble Deep Fields (HDFs) while the deep fields co-added over time are  $\sim 1.5$  magnitudes deeper than the HDFs (Williams et al. 1996) and up to 0.5 magnitudes deeper than the UDF depending on the filter. SNAP has the additional advantage of having nine filters ob-

TABLE 9  
THE SNAP AB MAGNITUDE SURVEY DEPTH FOR A POINT SOURCE  $S/N = 5$ .<sup>a</sup>

Filter	$\lambda_{eff}(\text{\AA})$	$\Delta\lambda(\text{\AA})$	Deep Survey (AB mag)		Wide-field Survey (AB mag)	Panoramic
			Per Scan	Co-added Scans		
1	4400	1000	27.9	30.6	28.3	26.7
2	5060	1150	27.9	30.6	28.3	26.8
3	5819	1322	27.8	30.5	28.2	26.8
4	6691	1520	27.8	30.4	28.1	26.8
5	7695	1749	27.8	30.4	28.1	26.8
6	8849	2011	27.7	30.3	28.0	26.7
7	10177	2313	27.5	30.1	27.8	26.6
8	11704	2660	27.5	30.1	27.8	26.6
9	13459	3059	27.4	30.0	27.7	26.5

<sup>a</sup>Random cosmic-ray hits make the  $S/N$  for a given position probabilistic; see text. The choice of filter set is currently subject to optimization studies; the filters and depths presented here are meant to be illustrative.

serving to this depth, compared to the four filters of the HDFs, and 9000 times the area in the deep survey; when these data from all filters are combined, the limiting magnitude increases by another 0.6 magnitudes. The wide-field survey has  $\sim 600,000$  times the area of the HDFs.

SNAP fields will contain many faint diffuse galaxies whose detection is important for the weak-lensing studies, and for other potential science projects. The limiting magnitudes for Gaussian-aperture photometry of an exponential-disk galaxy with  $\text{FWHM}=0.12''$  are shown in Table 10.

## 8.2. Ancillary Science

In this section we give a brief outline of additional science topics likely to benefit from SNAP survey data. This list is incomplete, and includes only a few of the most obvious ancillary science projects.

The SDSS (York et al. 2000), Hubble Deep Fields (HDFs) (Williams et al. 1996, 2000), and Ultra Deep Field<sup>4</sup> demonstrate the vast range of science enabled by wide, deep, and precise multi-band surveys. SNAP will carry this tradition forward as the first wide field survey in space.

SNAP deep-survey fields will cover more than 9000

times the area of the HDFs, go even deeper, include 9 color observations, and provide significant time domain information. The SNAP wide-survey field is comparable in size to the Sloan Southern Survey<sup>5</sup> and CFHT Legacy Survey<sup>6</sup> but includes diffraction limited imaging, and probes many magnitudes fainter in more filters. A panoramic survey would cover almost a quarter of the full sky at slightly shallower depth. The combination of depth, temporal coverage, wavelength range, diffraction-limited seeing, and wide field make SNAP imaging surveys uniquely powerful in the study of a wide range of objects and phenomena, which we outline below.

- Galaxies — Within the 15 square degree deep survey area, SNAP will make accurate ( $\Delta_z < 0.03$ ) photometric redshift estimates for at least  $10^7$  galaxies from redshift 0 to 3.5, spanning more than 90% of the age of the Universe. Statistical studies are possible with such a large sample, e.g. the determination of the galaxy luminosity function and color distributions as a function of redshift. Photometric redshifts can be estimated from the 4000 Å break for galaxies out to about  $z = 3.2$ . For galaxies at still higher redshift, the simplest indicator is the Ly-

<sup>4</sup><http://www.stsci.edu/hst/udf>

<sup>5</sup><http://www.sdss.org>

<sup>6</sup><http://www.cfht.hawaii.edu/CFHLS>

TABLE 10  
 THE SNAP AB MAGNITUDE SURVEY DEPTH FOR AN EXPONENTIAL-DISK GALAXY HAVING FWHM=0.12”  
 FOR  $S/N = 10$ .<sup>a</sup>

Filter	$\lambda_{eff}(\text{\AA})$	$\Delta\lambda(\text{\AA})$	Deep Survey (AB mag)		Wide-field Survey (AB mag)	Panoramic
			Per Scan	Co-added Scans		
1	4400	1000	26.4	29.0	26.8	25.2
2	5060	1150	26.3	28.9	26.7	25.3
3	5819	1322	26.3	28.9	26.6	25.3
4	6691	1520	26.2	28.8	26.6	25.3
5	7695	1749	26.3	28.9	26.6	25.3
6	8849	2011	26.2	28.8	26.5	25.3
7	10177	2313	26.2	28.8	26.5	25.3
8	11704	2660	26.2	28.8	26.5	25.3
9	13459	3059	26.1	28.7	26.5	25.3

<sup>a</sup>Random cosmic-ray hits make the  $S/N$  for a given position probabilistic; see text. The choice of filter set is currently subject to optimization studies; the filters and depths presented here are meant to be illustrative.

man break. For SNAP, the Lyman break enters the optical imager around redshift 3. In principle it can be followed using SNAP data beyond redshift 10, allowing identification of extremely high-redshift galaxies. The magnitude depth also allows discovery of low-surface-brightness and very high-redshift galaxies. High-resolution images will provide a view of the internal structure of galaxies and their interactions with each other. This data set, which will include morphological information for every object, will provide a unique opportunity to study the evolution of galaxies. The flood of galaxy evolution papers based on the Hubble Deep Fields points the way to what will be possible with the SNAP imaging data set.

- Galaxy structure formation — The wide-field surveys from SNAP offer an excellent opportunity to study galaxy clustering and its evolution at high redshifts ( $\approx 0.3 - 3$ ). This is a regime which is both especially interesting and rather poorly understood. There are some measurements of galaxy clustering at high redshift (Steidel et al. 1996), but these are severely limited by sample variance (Somerville et al. 2004). SNAP, increasing the size of high redshift surveys by several orders of magnitude, will be sub-

stantially less sensitive to cosmic variance. Photometric redshifts greatly enhance this work, allowing detailed study of the evolution of galaxy clustering.

- Galaxy clusters — Galaxy clusters, the most massive bound objects in the Universe, provide important probes of our understanding of structure formation (Evrard 1989). Constraining their formation and evolution is an important observational goal for the coming decade. Recent advances have overcome earlier limitations of optically selected cluster samples, essentially by using photometric redshift information to eliminate projection effects (Gladders & Yee 2000; Bahcall et al. 2003). Hubble Volume  $\Lambda$ CDM simulations (Evrard et al. 2002) predict that the SNAP surveys will provide detailed information on tens of thousands of galaxy clusters with masses above  $5 \times 10^{13} M_{\odot}$ . With NIR sensitivity, SNAP will allow sensitive detection of galaxy clusters all the way back to their earliest appearance around  $z = 2$ . The overall number of galaxy clusters is exponentially sensitive to the amplitude of initial density fluctuations.
- Quasars — Quasars are identified in multi-color imaging surveys by their non-stellar colors. This

- method has been shown by the Sloan Digital Sky Survey to be extremely effective at identifying quasars to redshift 6 and beyond. SDSS quasar discovery is limited to redshift 6.4 by the CCD sensitivity cutoff at  $1.0 \mu\text{m}$  (Pentericci et al. 2002). The most distant SDSS quasar, at redshift 6.42 (Fan et al. 2003), has a  $z$ -band magnitude of 20. By probing to wavelengths 1.7 times greater, and to depths 9 magnitudes fainter, SNAP will be able to detect quasars to redshift 10, and to probe the quasar luminosity function to 100 times fainter than the brightest quasars. SNAP's ability to identify diffuse objects associated with quasars may present interesting opportunities for the study of galaxy formation.
- Gamma-ray burst afterglows — Current evidence suggests that gamma-ray bursts are associated with the collapse of massive stars which live short lives and die where they are born. As a result, GRB's may trace the cosmic star formation rate. If so, there should be GRB's essentially coincident with the epoch of formation of the first stars. The most distant GRB known occurred at redshift of 4.5 (Andersen et al. 2000). SNAP will be able to identify GRB afterglows, and the orphan afterglows predicted by some models of beaming in GRB's to  $z = 10$ . Such orphan afterglows may even be detected as backgrounds to the SNe search.
  - Reionization history — The Universe became neutral at the time of recombination, around  $z = 1000$ , and the thermal radiation from that epoch travels to us undisturbed as the cosmic microwave background radiation. The lack of a Gunn-Peterson effect in the spectra of most quasars demonstrates that the Universe was reionized at some time between  $z = 1000$  and  $z = 6$ . The source of the ionizing radiation is the subject of substantial speculation. The recent discovery of an apparent Gunn-Peterson trough in the spectra of several  $z > 6$  SDSS quasars may provide the first glimpse of the epoch of reionization (White et al. 2003). By identifying many quasars and galaxies to  $z = 10$ , SNAP will set the stage for mapping the epoch of reionization in unprecedented detail. In combination with ground based and JWST spectroscopy, it will enable measurements of the proximity effect and studies of the spatial structure of reionization.
  - Transients/Variables — The discovery and observation of SNe Ia are the primary goals of SNAP, but transient “backgrounds” are interesting in their own right: quasars, active-galactic-nuclei, gamma-ray-burst optical counterparts, supernovae of other types, variable stars, and eclipsing binaries. Of particular interest to cosmology are time-delay measurements of the large expected number of strongly lensed variables (Blandford & Koopmans 2001). Gravitational microlensing studies of stars and quasars as probes of compact dark matter are also possible.
  - Stars — Faint limiting magnitudes and excellent star-galaxy separation will yield faint dwarf and halo stars. Proper motion can be detected with high-resolution and a long time reference. SNAP's accurate colors will yield excellent photometric parallaxes to all stars in the field. The geometry and substructure of the Galactic halo and disk in the direction of the SNAP fields can be mapped. Of particular interest would be a census of low-mass L and T stars and brown dwarfs throughout the Milky Way disk (Leggett et al. 2000).
  - Solar-system objects — The peculiar motion and parallax in the time-series data will facilitate the identification of local objects such as asteroids and Kuiper-belt objects. SNAP time series data will provide an excellent probe of faint, red objects in the Kuiper belt and beyond. A 2-3 month dedicated ecliptic survey with the SNAP survey would detect 10–50,000 Kuiper belt objects down to the size of the Comet Halley's nucleus.
  - Weak gravitational lensing — The importance of weak gravitational lensing for dark energy is described in §3. Weak gravitational lensing is also a powerful tool in mapping the distribution of mass in the Universe. Maps reconstructed from the observed shear field are sensitive to any mass along a given line of sight, regardless of its nature or state allowing dark matter mapping and the unbiased detection of galaxy clusters and their mass. The high surface density of resolved background galaxies enables the

construction of both two- and three-dimensional maps of the foreground dark matter distribution. In addition to providing further constraints upon cosmological parameters, these maps trace the growth of structure in the Universe and can be used to study the bias between mass and light through comparison with the galaxy distribution.

In recent years many groups have measured the shape distortions of field galaxies due to weak lensing and used these shear measurements to set constraints on cosmological parameters. In a number of weak-lensing surveys using ground and space-based data the second moment of the shear field has provided a constraint on the matter power spectrum, in particular on the quantity  $\Omega_M \sigma_8^{0.5}$ , that is comparable to the constraints set by more traditional methods such as the abundance of X-ray clusters. Current weak-lensing surveys seeking to measure higher order moments of the shear field and the magnification of background galaxies promise to provide an independent measure of  $\Omega_M$ , thus breaking the degeneracy between  $\Omega_M$  and  $\sigma_8$ , where  $\sigma_8$  is the amplitude of mass fluctuations on the scale  $8h^{-1}$  Mpc.

Precise photometric redshifts enable the making of 2-dimensional mass maps in multiple redshift slices, and even 3-dimensional mass reconstructions. This redshift tomography is much less effective from the ground because of the lower surface density of resolved galaxies, and cannot be extended as far. Space-based imaging is needed to resolve sufficiently many source galaxies at  $z > 1$  and follow the growth of structure at those redshifts. Furthermore, high-resolution images coupled with photometric redshifts permit the use of a recently formulated approach to 3-D mapping (Taylor 2001) which recreates the full 3-D mass distribution by simultaneously considering both the shear estimator and the photometric redshift of a galaxy. Applied to the SNAP deep survey, this technique will detect mass overdensities with a  $1\sigma$  sensitivity of  $10^{13} M_\odot$  (1/5 the mass of the Virgo cluster) at  $z = 0.25$ .

- Strong gravitational lensing — The high spatial resolution of SNAP NIR observations will enable the discovery of a large number of new

strong lenses (Kuhlen et al. 2004). The statistics from such a large, uniformly selected sample would be ideal to impose constraints on the density profiles of galaxies and clusters, as well as to constrain cosmological parameters beyond those of dark energy. The NIR observations, which are much less sensitive to dust extinction within the lens galaxy, are especially important in regard to strong lensing observations. Goobar et al. (2002b) find that assuming a flat universe, the statistical uncertainty on the mass density is  $\sigma_{\Omega_M}^{\text{stat}} \lesssim 0.05$ , although uncertainty of the lens modeling are likely to dominate.

The SDSS demonstrates clearly the way in which a wide-field survey can produce scientific yield well beyond its primary design goals. Individual objects found on SDSS images are routinely observed spectroscopically at the largest telescopes in the world, fulfilling the historical trend of wide-field small-aperture telescope imaging feeding targets for large-aperture telescope spectroscopy. The SNAP surveys will provide a similar opportunity in working with JWST and the next generation of ground-based extremely large telescopes.

## 9. Conclusion

The discoveries of recent years make this a fascinating new era of empirical cosmology, in which we are developing new technologies and instrumentation capable of addressing fundamental questions. The extraordinary challenge of the precision and accuracy necessary to explore the properties of dark energy requires a new stringent data set in order to improve statistical uncertainties and control systematic uncertainties; large numbers of supernovae over an extended redshift range with light curves and spectra measured to high signal-to-noise and deep, wide fields full of weak-lensed galaxies with high-resolution PSFs with unprecedented stability.

Based on these data requirements, we have developed a reference mission called the Supernova / Acceleration Probe, consisting of a detailed observing program carried out with an optimized wide-field telescope and attendant imaging and spectrograph instruments. The optical, mechanical, and thermal studies and analyses conducted to date indicate that the reference model is manufacturable and testable using proven techniques. The imager will provide PSF-controlled wide-field images of galaxies with effi-

cient multiplexed supernova discovery and light-curve building while the spectrograph satisfies the performance requirements for measuring key spectral features of the faintest supernovae.

The reference model presented in this paper addresses the many requirements necessary for a high-precision supernova experiment, a PSF-controlled weak-lensing experiment, and makes possible a range of further complementary dark-energy studies. We use numerical simulations and trade studies to refine the mission concept and quantify the expected science yield of SNAP. This paper will be followed up with further results of these studies and the progress in the optimization of SNAP.

Although SNAP is designed as a self-contained experiment, its surveys can be used in conjunction with complementary ground-based and JWST-based studies that can further strengthen the reference SNAP mission.

SNAP presents a unique opportunity to probe the dark energy and advance our understanding of the Universe. Moreover, the principal survey missions of SNAP will produce a cornucopia of observations capable of revolutionizing other areas of astrophysics and cosmology. After completion of these primary missions, a guest survey program is envisioned filling the remaining satellite lifetime to allow the full potential of SNAP to be realized.

### Acknowledgments

We thank Masahiro Takada for making detailed results of his work available. This work was supported by the Director, Office of Science, of the U.S. Department of Energy under Contract No. DE-AC03-76SF00098.

### REFERENCES

Abazajian, K. & Dodelson, S. 2003, *Physical Review Letters*, 91, 41301  
 Abazajian, K. et al. 2003, *AJ*, 126, 2081  
 Aguirre, A. 1999, *ApJ*, 512, L19  
 Aguirre, A. & Haiman, Z. 2000, *ApJ*, 532, 28  
 Aldering, G., Knop, R., & Nugent, P. 2000, *AJ*, 119, 2110  
 Aldering, G. et al. 2002, *Proc. SPIE*, 4836, 61

Allen, S. W., Schmidt, R. W., Fabian, A. C., & Ebeling, H. 2003, *MNRAS*, 342, 287  
 Amanullah, R., Mörtzell, E., & Goobar, A. 2003, *A&A*, 397, 819  
 Andersen, M. I. et al. 2000, *A&A*, 364, L54  
 Bahcall, N. A., Ostriker, J. P., Perlmutter, S., & Steinhardt, P. J. 1999, *Science*, 284, 1481  
 Bahcall, N. A. et al. 2003, *ApJS*, 148, 243  
 Balbi, A. et al. 2000, *ApJ*, 545, L1  
 Baron, E., Hauschildt, P. H., Branch, D., Wagner, R. M., Austin, S. J., Filippenko, A. V., & Matheson, T. 1993, *ApJ*, 416, L21  
 Baron, E. et al. 1995, *ApJ*, 441, 170  
 Bebek, C. J. et al. 2002a, *Proc. SPIE*, 4669, 161  
 —. 2002b, *IEEE Trans. Nucl. Sci.*, 49, 1221  
 Bennett, C. L. et al. 2003, *ApJS*, 148, 1  
 Bernstein, G. 2002, *PASP*, 114, 98  
 Bernstein, G. & Jain, B. 2004, *ApJ*, 600, 17  
 Bernstein, G. & Kim, A. 2004, in preparation  
 Bessell, M. S. 1990, *PASP*, 102, 1181  
 Blandford, R. D. & Koopmans, L. V. E. 2001, *Bulletin of the American Astronomical Society*, 33, 1481  
 Bohlin, R. C., Dickinson, M. E., & Calzetti, D. 2001, *AJ*, 122, 2118  
 Borys, C., Chapman, S. C., Halpern, M., & Scott, D. 2002, *MNRAS*, 330, L63  
 Bowen, I. S. 1938, *ApJ*, 88, 113  
 Branch, D., Perlmutter, S., Baron, E., & Nugent, P. 2001, *ArXiv Astrophysics e-prints*, astro-ph/0109070  
 Branch, D. & van den Bergh, S. 1993, *AJ*, 105, 2231  
 Brax, P. & Martin, J. 2000, *Phys. Rev.*, D61, 103502  
 Caldwell, R. R., Davé, R., & Steinhardt, P. J. 1998, *Phys. Rev. Lett.*, 80, 1582  
 Cardelli, J. A., Clayton, G. C., & Mathis, J. S. 1989, *ApJ*, 345, 245

- Carroll, S. M., Duvvuri, V., Trodden, M., & Turner, M. S. 2003, ArXiv Astrophysics e-prints, astro-ph/0306438
- Coble, K., Dodelson, S., & Frieman, J. A. 1997, Phys. Rev. D, 55, 1851
- Content, R. 1997, Proc. SPIE, 2871, 1295
- Cooray, A., Huterer, D., & Baumann, D. 2004, Phys. Rev. D, 69, 027301
- Couch, W. J. et al. 1989, in Particle Astrophysics: Forefront Experimental Issues, 192
- Dvali, G., Gabadadze, G., & Porrati, M. 2000, Phys. Rev. B, 485, 208
- Ealet, A. et al. 2003, Proc. SPIE, 4850
- Efstathiou, G. et al. 2002, MNRAS, 330, L29
- Evrard, A. E. 1989, ApJ, 341, L71
- Evrard, A. E. et al. 2002, ApJ, 573, 7
- Fan, X. et al. 2003, AJ, 125, 1649
- Ferreira, P. G. & Joyce, M. 1998, Phys. Rev. D, 58, 23503
- Frieman, J. A., Hill, C. T., Stebbins, A., & Waga, I. 1995, Phys. Rev. Lett., 75, 2077
- Frieman, J. A., Huterer, D., Linder, E. V., & Turner, M. S. 2003, Phys. Rev. D, 67, 83505
- Garnavich, P. M. et al. 1998, ApJ, 509, 74
- Gladders, M. D. & Yee, H. K. C. 2000, AJ, 120, 2148
- Goldhaber, G. et al. 2001, ApJ, 558, 359
- Goobar, A., Bergström, L., & Mörtzell, E. 2002a, A&A, 384, 1
- Goobar, A., Mörtzell, E., Amanullah, R., & Nugent, P. 2002b, A&A, 393, 25
- Goobar, A. & Perlmutter, S. 1995, Ap. J., 450
- Groom, D. E. et al. 2000, Nuclear Instruments and Methods in Physics Research A, 442, 216
- Haiman, Z., Mohr, J. J., & Holder, G. P. 2001, ApJ, 553, 545
- Hamuy, M., Phillips, M. M., Suntzeff, N. B., Schommer, R. A., Maza, J., & Aviles, R. 1996a, AJ, 112, 2391
- Hamuy, M., Trager, S. C., Pinto, P. A., Phillips, M. M., Schommer, R. A., Ivanov, V., & Suntzeff, N. B. 2000, AJ, 120, 1479
- Hamuy, M. et al. 1996b, AJ, 112, 2408
- Hatano, K., Branch, D., & Deaton, J. 1998, ApJ, 502, 177
- Hatano, K., Branch, D., Lentz, E. J., Baron, E., Filippenko, A. V., & Garnavich, P. M. 2000, ApJ, 543, L49
- Hawkins, E. et al. 2003, MNRAS, 346, 78
- Hayes, D. S. 1985, in IAU Symp. 111: Calibration of Fundamental Stellar Quantities, ed. D. S. Hayes, L. E. Pasinetti, & A. G. D. Philip, 225–249
- Hayes, D. S. & Latham, D. W. 1975, ApJ, 197, 593
- Höflich, P., Gerardy, C., Linder, E., & Marion, H. 2003, in Stellar candles for the extragalactic distance scale, ed. D. Alloin & W. Gieren, Lecture notes in physics, 0075-8450 ;635 (Springer)
- Höflich, P., Wheeler, J. C., & Thielemann, F. K. 1998, ApJ, 495, 617
- Holland, S. E., Groom, D. E., Palaio, N. P., & Stover, R. J. and Wei, M. 2003, IEEE Trans. Elec. Dev., 50(1), 225
- Holz, D. E. 2001, ApJ, 556, L71
- Holz, D. E. & Wald, R. M. 1998, PRD, 58, 063501
- Hu, W. 1999, ApJ, 522, L21
- Huterer, D. 2002, Phys. Rev. D, 65, 63001
- Huterer, D. & Cooray, A. 2004, ArXiv Astrophysics e-prints, astro-ph/0404062
- Huterer, D., Kim, A., Krauss, L. M., & Broderick, T. 2004, ArXiv Astrophysics e-prints, astro-ph/0402002
- Huterer, D. & Starkman, G. 2003, Phys. Rev. Lett., 90, 031301
- Huterer, D. & Turner, M. S. 2001, Phys. Rev. D, 64, 123527

- Jain, B. & Taylor, A. 2003, *Physical Review Letters*, 91, 141302
- Kaiser, N. 1998, *ApJ*, 498, 26
- Kim, A., Goobar, A., & Perlmutter, S. 1996, *PASP*, 108, 190
- Kim, A. G., Linder, E. V., Miquel, R., & Mostek, N. 2004, *MNRAS*, 347, 909
- Kirshner, R. P. & Kwan, J. 1974, *ApJ*, 193, 27
- Knop, R. A. et al. 2003, *ApJ*, 598, 102
- Korsch, D. 1977, *ApOpt*, 16, 2074
- Kuhlen, M., Keeton, C. R., & Madau, P. 2004, *ApJ*, 601, 104
- Kujat, J., Linn, A. M., Scherrer, R. J., & Weinberg, D. H. 2002, *ApJ*, 572, 1
- Lampton, M. L. et al. 2002a, *Proc. SPIE*, 4854, 632
- . 2002b, *Proc. SPIE*, 4849, 215
- . 2003, *Proc. SPIE*, 5166
- Lange, A. E. et al. 2001a, *Phys. Rev. D*, 63, 42001
- . 2001b, *Phys. Rev. D*, 63, 42001
- Leggett, S. K. et al. 2000, *ApJ*, 536, L35
- Lentz, E. J., Baron, E., Branch, D., Hauschildt, P. H., & Nugent, P. E. 2000, *ApJ*, 530, 966
- Leonard, D. C., Kanbur, S. M., Ngeow, C. C., & Tanvir, N. R. 2003, *ApJ*, 594, 247
- Linder, E. V. 2003a, *Phys. Rev. Lett.*, 90, 91301
- . 2003b, *ArXiv Astrophysics e-prints*, astro-ph/0311403
- . 2004, *ArXiv Astrophysics e-prints*, astro-ph/0402503
- Linder, E. V. & Huterer, D. 2003, *Phys. Rev. D*, 67, 81303
- Mörtsell, E. & Goobar, A. 2003, *Journal of Cosmology and Astro-Particle Physics*, 9, 9
- Mörtsell, E., Goobar, A., & Bergström, L. 2001, *ApJ*, 559, 53
- Madau, P., della Valle, M., & Panagia, N. 1998, *MNRAS*, 297, L17
- Massey, R. et al. 2004, *AJ*, accepted
- Matsubara, T. & Szalay, A. S. 2003, *Phys. Rev. Lett.*, 90, 021302
- Norgaard-Nielsen, H. U., Hansen, L., Jorgensen, H. E., Aragon Salamanca, A., & Ellis, R. S. 1989, *Nature*, 339, 523
- Nugent, P., Kim, A., & Perlmutter, S. 2002, *PASP*, 114, 803
- Nugent, P., Phillips, M., Baron, E., Branch, D., & Hauschildt, P. 1995, *ApJ*, 455, L147
- Pain, R. et al. 2002, *ApJ*, 577, 120
- Pentericci, L. et al. 2002, *AJ*, 123, 2151
- Percival, W. J. et al. 2002, *MNRAS*, 337, 1068
- Perlmutter, S. 1999, *FNAL Inner Space/Outer Space II Symposium*
- Perlmutter, S. & Schmidt, B. P. 2003, *ArXiv Astrophysics e-prints*, astro-ph/0303428
- Perlmutter, S., Turner, M. S., & White, M. 1999a, *Phys. Rev. Lett.*, 83, 670
- Perlmutter, S. et al. 1995, *ApJ*, 440, L41
- . 1997, *ApJ*, 483
- . 1998, *Nature*, 391
- . 1999b, *ApJ*, 517, 565
- Phillips, M. M. 1993, *ApJ*, 413, L105
- Phillips, M. M., Lira, P., Suntzeff, N. B., Schommer, R. A., Hamuy, M., & Maza, J. 1999, *AJ*, 118, 1766
- Prieto, E. et al. 2002, *Proc. SPIE*, 4850
- Ratra, B. & Peebles, P. J. E. 1988, *Phys. Rev. D*, 37, 3406
- Refregier, A. 2003, *ARA&A*, 41, 645
- Refregier, A. et al. 2004, *AJ*, accepted
- Rhodes, J., Refregier, A., & Groth, E. J. 2000, *ApJ*, 536, 79
- Rhodes, J. et al. 2004, *Astroparticle Physics*, 20, 377

- Riess, A. G., Press, W. H., & Kirshner, R. P. 1996, *ApJ*, 473, 88
- Riess, A. G. et al. 1998, *AJ*, 116, 1009
- . 1999, *AJ*, 117, 707
- . 2004, *ApJ*, 600, L163
- Schlegel, D. J., Finkbeiner, D. P., & Davis, M. 1998, *ApJ*, 500, 525
- Schmidt, B. P. et al. 1998, *ApJ*, 507, 46
- Scott, S. E. et al. 2002, *MNRAS*, 331, 817
- Seo, H. & Eisenstein, D. J. 2003, *ApJ*, 598, 720
- Somerville, R. S., Lee, K., Ferguson, H. C., Gardner, J. P., Moustakas, L. A., & Giavalisco, M. 2004, *ApJ*, 600, L171
- Spergel, D. N. et al. 2003, *ApJS*, 148, 175
- Steidel, C. C., Giavalisco, M., Pettini, M., Dickinson, M., & Adelberger, K. L. 1996, *ApJ*, 462, L17
- Stover, R. J. et al. 2000, in *Optical Detectors for Astronomy II: State-of-the-Art at the Turn of the Millennium*, 239
- Sullivan, M. et al. 2003, *MNRAS*, 340, 1057
- Takada, M. & Jain, B. 2003, *MNRAS*, 344, 857
- Taylor, A. N. 2001, *ArXiv Astrophysics e-prints*, astro-ph/0111605
- Tegmark, M. 2002, *Phys. Rev. D*, 66, 103507
- Tonry, J. L. et al. 2003, *ApJ*, 594, 1
- Turner, M. S. & White, M. 1997, *Phys. Rev. D*, 56, 4439
- Vilenkin, A. 1984, *Phys. Rev. Lett.*, 53, 1016
- Vilenkin, A. & Shellard, E. 1994, *Cosmic Strings and other Topological Defects* (Cambridge, U.K.: Cambridge University Press)
- Walder, J.-P., Chao, G., Genat, J., Karcher, A., Steckert, J., & von der Lippe, H. 2003, *IEEE Trans. Nucl. Sci.*, In press
- Weller, J. & Albrecht, A. 2001, *Phys. Rev. Lett.*, 86, 1939
- . 2002, *Phys. Rev. D*, 65, 3512
- White, R. L., Becker, R. H., Fan, X., & Strauss, M. A. 2003, *AJ*, 126, 1
- Williams, R. E. et al. 1996, *AJ*, 112, 1335
- . 2000, *AJ*, 120, 2735
- York, D. G. et al. 2000, *AJ*, 120, 1579